A 4D-Var inversion system based on the icosahedral grid model (NICAM-TM 4D-Var v1.0): 2. Optimization scheme and identical twin experiment of atmospheric CO$_2$ inversion

Yosuke Niwa[1], Yosuke Fujii[1], Yousuke Sawa[1], Yosuke Iida[2], Akihiko Ito[3], Masaki Satoh[4,5],
Ryoichi Imasu[4], Kazuhiro Tsuboi[1], Hidekazu Matsueda[1], and Nobuko Saigusa[3]

[1]Oceanography and Geochemistry Research Department, Meteorological Research Institute, Tsukuba, Japan
[2]Global Environment and Marine Department, Japan Meteorological Agency, Tokyo, Japan
[3]Center for Global Environmental Research, National Institute for Environmental Studies, Tsukuba, Japan
[4]Atmosphere and Ocean Research Institute, The University of Tokyo, Kashiwa, Japan
[5]Japan Agency for Marine-Earth Science and Technology, Yokohama, Japan

Correspondence to: Y. Niwa (yniwa@mri-jma.go.jp)

Abstract. A 4-dimensional variational method (4D-Var) is a popular technique for inverse modeling of atmospheric constituents, but it is not without problems. Using an icosahedral grid transport model and the 4D-Var method, a new atmospheric greenhouse gas (GHG) inversion system has been developed. The system combines off-line forward and adjoint models with a quasi-Newton optimization scheme. The new approach is then used to conduct identical twin experiments to investigate optimal system settings for an atmospheric CO$_2$ inversion problem, and to demonstrate the validity of the new inversion system. It is found that a system of forward and adjoint models that has less model errors but with non-linearity performs better than another system that conserves linearity with exact adjoint relationship. Furthermore, the effectiveness of the prior error correlations is confirmed; the global error is reduced by about 15 % by adding prior error correlations that are simply designed. With the optimal setting, the new inversion system successfully reproduces the spatiotemporal variations of the surface fluxes, from regional (such as biomass burning) to a global scale. The optimization algorithm introduced in the new system does not require difficult decomposition of a matrix that establishes the correlation among the prior flux errors. This enables us to design the prior error covariance matrix more freely.

1 Introduction

Using the Bayesian algorithm, an inverse model estimates spatiotemporal variations of surface fluxes from the observations of atmospheric concentrations with help of a priori information. A power of such technique has been demonstrated in previous studies, such as the synthesis inversion analysis by Peylin et al. (2013) that demonstrated significant variations in regional carbon budgets at seasonal to interannual time scales.

In this study, we have developed a new inversion system based on the 4-dimensional variational (4D-Var) method. The 4D-Var method is a popular inversion method and has been widely used in inversion studies for atmospheric carbon dioxide (CO$_2$)

(e.g. Chevallier et al., 2005; Rödenbeck, 2005; Baker et al., 2006a), methane (CH_4) (e.g. Bergamaschi et al., 2013) and carbon monoxide (CO) (e.g. Kopacz et al., 2010; Hooghiemstra et al., 2012).

Our primary interests are in long-lived greenhouse gases (GHGs) such as CO_2 and CH_4. Owing to strong requirement for high-precision measurements necessary to identify changes in surface fluxes, observations of such atmospheric constituents

5 had been quite limited. In the beginning, flask air sampling was adopted mostly at background sites, with a typical weekly sampling frequency (e.g. Conway et al., 1994). These data have been used in a synthesis inversion method (Enting, 2002) to estimate sub-continental scale CO_2 fluxes (e.g. Rayner et al., 1999; Gurney et al., 2002; Baker et al., 2006b). In recent decades, the global observation network of atmospheric GHGs has significantly expanded to include various measurement platforms. For example, *in situ* continuous observation measurements are now regularly taken at background stations, as well

10 as at tall towers to infer regional continental fluxes (e.g. Sasakawa et al., 2010; Andrews et al., 2014). Moreover, worldwide aircraft observation programs are now regularly conducted (e.g. Machida et al., 2008; Sawa et al., 2015; Matsueda et al., 2015), along with satellite observations dedicated to measurements of GHGs (Yoshida et al., 2013; Saitoh et al., 2016). These numerous GHG observational data can be exploited to estimate surface fluxes on a much finer scale than a sub-continental scale. While the synthesis inversion method has limitations in resolution, both in fluxes and observations owing to its direct

15 matrix calculation approach, the 4D-Var method has nearly no limitation in the number of observations it can accommodate. The method also has the ability to estimate model grid resolution fluxes, so that regionally limited CO_2 flux anomalies such as biomass burnings are detectable. The 4D-Var method was developed originally for numerical weather prediction (NWP), in which a weather model's initial state of the atmosphere is optimized, with respect to a set of observations, to improve weather prediction. This is done over successive time windows. At present, the 4D-Var method is employed in many leading operational

20 NWP centers. However, because of a much longer assimilation window and the requirement of optimizing boundary conditions (surface fluxes), but not the model's initial conditions, application of the 4D-Var method to GHGs inversion raises different issues from those associated with NWP and need to be resolved.

In developing our 4D-Var inversion system, we have introduced unique numerical techniques that have not been used in previous 4D-Var inversions of GHGs; these techniques use an icosahedral grid transport model based on Non-hydrostatic

25 Icosahedral Atmospheric Model (NICAM: Tomita and Satoh, 2004; Satoh et al., 2008, 2014), along with an efficient optimization scheme of Preconditioned Optimizing Utility for Large-dimensional analyses (POpULar: Fujii and Kamachi, 2003; Fujii, 2005). NICAM is one of the most advanced general circulation models (GCMs), with its dynamical frame structured with quasi-homogenous grids that are made by recursively dividing an icosahedron, which is completely different from the regular latitude-longitude grid models used so far. For the new inversion system, we have employed the NICAM-based Trans-

30 port Model (NICAM-TM), naming our inversion system as NICAM-TM 4D-Var. The previous accompanying paper of Niwa et al. (2016) derived and evaluated the off-line forward and adjoint models of NICAM-TM. This paper describes the entire NICAM-TM 4D-Var system, including the optimization scheme POpULar.

One prominent feature of POpULar is that it does not require inverse calculation of the prior error covariance. Generally, an inverse matrix of a prior error covariance is included in the Bayesian inversion algorithm. However, its direct calculation

35 is infeasible due to its large matrix size. Therefore, previous studies have avoided the inverse matrix calculation by simply

neglecting the off-diagonal elements of the prior error covariance or employing eigenvalue decomposition (Chevallier et al., 2007; Meirink et al., 2008). Actually, the off-diagonal elements represent the error correlation among prior fluxes. In NWP, the spectral method is often used and the prior error covariance is defined in the spectral field, ~~thus able to regard~~ the prior error covariance as diagonal. However, it cannot be applied to the flux inversion problem. Although designing flux error correlations

5   is not a trivial task, it needs to be addressed because surface fluxes must be mutually correlated when they are located in a close proximity to each other (Chevallier et al., 20   ). Additionally, it is possible that the error correlations could more effectively propagate observational information to estimated flux values. However, eigenvalue decomposition would become difficult when the specified prior error covariance is complicated or when the spatiotemporal resolution of fluxes is increased. Since the POpULar optimization scheme does not require eigenvalue decomposition, we can easily introduce flux error correlations into

10   the inverse calculation. POpULar was developed originally for oceanography assimilation (Usui et al., 2006, 2015); our study is its first application to an inverse problem ~~of atmospheric trace constituent~~.

In order to validate and verify the new inversion system, we have conducted identical twin experiments of atmospheric CO_2 inversion, in which pseudo observations produced by "true fluxes" are assimilated, instead of real observations. It has been demonstrated that such an identical twin experiment is an effective way to test the ability of an optimization scheme in

15   an inversion calculation (e.g. Baker et al., 2006a; Chevallier et al., 2007; Yumimoto and Takemura, 2013; Liu et al., 2014). Conducting sensitivity tests based on the identical experiment, we investigate the optimal system settings in the context of adjoint models and optimization schemes. In addition, we demonstrate the utility of introducing error correlations in the prior fluxes.

As described in Niwa et al. (2016), NICAM-TM has two types of adjoint models: one is a discrete adjoint model and the

20   other is a continuous one. The discrete adjoint model ensures model linearity and maintains an exact adjoint relationship with its corresponding forward model, while the continuous adjoint model is non-linear and consequently loses the exact adjoint relationship but has less model errors. Gou and Sandu (2011) compared a continuous adjoint model with a corresponding discrete adjoint model using a regional chemical transport model and evaluated the effect of using these two models in the optimization of initial states of tropospheric ozone. In that study, they found continuous adjoint to be superior in ideal assimi-

25   lation cases, especially when observations are sparse. However, when real observations were used in assimilation, they found that the discrete adjoint performed better than the continuous adjoint. Therefore, which adjoint is better depends strongly on models ~~used.~~ Furthermore, it may also depend on the assimilation settings. Approaching the problem differently from Gou and Sandu (2011) when applied to CO_2, we try to optimize surface fluxes of CO_2, which has a much longer lifetime in the atmosphere and hence requires a longer assimilation window than ozone. In this study, we evaluate the effect of using discrete

30   and continuous adjoint models as applied to CO_2 inversion problems. Using the optimal inversion settings determined from the sensitivity tests, we also investigate how the current observation network could be exploited better to constrain surface flux estimates.

2   Methods

2.1   NICAM-TM 4D-Var

2.1.1   System overview

An inversion problem employs Bayes' theorem, and an optimal solution of control variable $\mathbf{x}$ is obtained where the cost function
defined below is minimized.

$$J(\mathbf{x}) = \frac{1}{2}\mathbf{x}^{\mathrm{T}}\mathbf{B}^{-1}\mathbf{x} + \frac{1}{2}\left(\mathbf{Mx} - \mathbf{y}^{\mathrm{dobs}}\right)^{\mathrm{T}}\mathbf{R}^{-1}\left(\mathbf{Mx} - \mathbf{y}^{\mathrm{dobs}}\right),$$ (1)

where $\mathbf{B}$ is the prior error covariance matrix of $\mathbf{x}$, $\mathbf{M}$ is the forward transport model operator matrix which links surface fluxes
to atmospheric concentration measurements taken at specified locations and time, and $\mathbf{R}$ is the error covariance matrix of the
misfit between observations and modeled concentrations. It should be noted here that $\mathbf{M}$ is assumed linear according to the
linear property of atmospheric transport, though we use both linear and non-linear models as described in Section 2.3 below.
The control variable vector $\mathbf{x}$ represents increment from the prior flux $\mathbf{x}^{\mathrm{pri}}$ and the observation vector $\mathbf{y}^{\mathrm{dobs}}$ represents differences
between the modeled concentrations from $\mathbf{x}^{\mathrm{pri}}$ and observed concentrations $\mathbf{y}^{\mathrm{obs}}$, i.e., $\mathbf{y}^{\mathrm{dobs}} = \mathbf{y}^{\mathrm{obs}} - \mathbf{Mx}^{\mathrm{pri}}$. In fact, the control
variable vector $\mathbf{x}$ consists of initial concentrations as well as surface fluxes, thus atmospheric concentration fields are uniquely
determined in the model. However, for simplicity, we only optimize surface fluxes in this study. In the 4D-Var method, the
optimal $\mathbf{x}$ is determined after iterative calculations that uses the gradient of the cost function with respect to $\mathbf{x}$

$$\mathbf{g} = \mathbf{B}^{-1}\mathbf{x} + \mathbf{M}^{\mathrm{T}}\mathbf{R}^{-1}\left(\mathbf{Mx} - \mathbf{y}^{\mathrm{dobs}}\right).$$ (2)

The last term on the right-hand side is derived by a forward simulation $\mathbf{Mx}$ followed by an adjoint simulation
$\mathbf{M}^{\mathrm{T}}\mathbf{R}^{-1}\left(\mathbf{Mx} - \mathbf{y}^{\mathrm{dobs}}\right)$, which are performed by the forward and adjoint models of NICAM-TM, respectively. Both the forward
and adjoint models are driven by archived meteorological data (e.g. mass fluxes, temperatures, turbulent coefficients, cumulus
base mass fluxes; details are found in Niwa et al. (2016)). The meteorological data are prepared by a GCM run of NICAM, in
which horizontal winds are nudged towards reanalysis data to simulate real atmospheric flow fields.

In summary, Fig. 1 shows a schematic figure of the NICAM-TM 4D-Var system. In practice, the 4D-Var calculations are
conducted as follows:

(i) Run the on-line NICAM with nudging to make meteorological data that are used in the following simulations of the
forward and adjoint NICAM-TM,

(ii) Run the forward NICAM-TM to calculate atmospheric concentration fields of a target atmospheric constituent forced by
prior flux data,

(iii) Calculate the differences between the modeled and observed concentrations,

(iv) Run the adjoint NICAM-TM to calculate the gradient of the cost function from the model-observation differences that
are weighted by the error covariance of observation-model misfit, and

(v) Modify the prior flux data according to the cost function and its gradient using the POpULar optimization scheme.

The prior flux data are replaced with those given by (v), and then the (ii)-(v) calculation steps are repeated until the flux data are sufficiently optimized. Finally, the optimized flux is ~~treated as~~ the posterior flux.

2.1.2 NICAM-TM

NICAM achieves consistency between tracer transport and air density change, which assures Lagrangian conservation and mass conservation simultaneously, owing to its finite volume method-based dynamical frame (Satoh et al., 2008; Niwa et al., 2011a). This property is absolutely necessary for transport simulations of long-lived tracers such as GHGs. Because of this, NICAM-TM has been developed and used for transport and inversion studies of CO_2 (Law et al., 2008; Patra et al., 2008; Niwa et al., 2011b, 2012; Peylin et al., 2013). Its fundamental transport performances have been evaluated satisfactorily using observations of radon (^{222}Rn) and sulfur hexafluoride (SF_6) (Niwa et al., 2011a, 2012).

Detail descriptions of the off-line forward and adjoint models of NICAM-TM are found in the accompanying paper of Niwa et al. (2016). Reanalysis data used with nudging in the on-line calculation are from the 6-hourly Japan Meteorological Agency Climate Data Assimilation System (JCDAS) reanalysis (Onogi et al., 2007). The archived meteorological data consist of air mass densities, three-dimensional air mass fluxes, vertical diffusion coefficients, mixing ratios of water substances, temperatures, and cumulus base mass fluxes. These data are consistent with the dynamical calculation of NICAM, though their temporal resolutions are decreased from the original model time step (20 min.) to 1- to 3-hourly steps in the off-line model calculations (Niwa et al., 2016). The horizontal resolution is set as "glevel-5" (5 denotes the number of division from the original icosahedron; see Fig. 1 of Niwa et al. (2016)), whose grid interval is about 240 km, and the number of vertical model layers is 40.

2.1.3 POpULar

For optimization, we use the scheme of POpULar (Fujii and Kamachi, 2003; Fujii, 2005). The POpULar scheme is based on the optimizing scheme developed by Derber and Rosati (1989) (hereafter DR89). Fujii and Kamachi (2003) extended the linear conjugate gradient method of DR89 to non-linear cases using a quasi-Newton method.

In Eqs. (1) and (2), the matrix size of $\mathbf{B}$ is too large to be inverted if $\mathbf{B}$ is an off-diagonal matrix, i.e., when prior error correlations are considered. Therefore, a transformation of the control variables is often applied, with one prominent transformation being $\tilde{\mathbf{x}} = \mathbf{B}^{-1/2}\mathbf{x}$. This transformation provides efficient preconditioning to accelerate the convergence of iterative calculations (Lorenc, 1988). In fact, several 4D-Var inversion systems for atmospheric trace gas constituents employ this transformation with eigenvalue decomposition (Chevallier et al., 2007; Meirink et al., 2008), though feasibility of eigenvalue decomposition still depends on the matrix size and the designing of the error correlations. In contrast, DR89 and POpULar also use the preconditioning of Lorenc (1988) but they do not require eigenvalue decomposition. Detailed algorithm of DR89 is described in Appendix A. Below we describe the POpULar scheme but readers are encouraged to ~~see~~ Fujii (2005) for further explanation.

The quasi-Newton scheme of POpULar employs the limited-memory version (Nocedal, 1980; Liu and Nocedal, 1989) of the Broyden-Fletcher-Goldfarb-Shanno formula (L-BFGS) that updates the search direction $\mathbf{d}$ of the control variable $\mathbf{x}$ using an approximated inverse Hessian of $J(\equiv \mathbf{H})$. Using the transformation of Lorenc (1988) ($\tilde{\mathbf{x}} = \mathbf{B}^{-1/2}\mathbf{x}$), the transformed control variable is updated in iterative calculations as

$$\tilde{\mathbf{x}}_k = \tilde{\mathbf{x}}_{k-1} + \alpha_k \tilde{\mathbf{d}}_{k-1}, \tag{3}$$

$$\tilde{\mathbf{d}}_k = -\tilde{\mathbf{H}}_{k,0}\tilde{\mathbf{g}}_k, \tag{4}$$

where k is the iteration counter, $\tilde{\mathbf{d}} = \mathbf{B}^{-1/2}\mathbf{d}$, $\tilde{\mathbf{g}} = \mathbf{B}^{1/2}\mathbf{g}$, and $\tilde{\mathbf{H}}_{k,0} = \mathbf{B}^{-1/2}\mathbf{H}_{k,0}\mathbf{B}^{-1/2}$. The coefficient α_k is the step length of the line search that minimizes $J(\mathbf{x}_{k-1} + \alpha_k \mathbf{d}_{k-1})$. If an optimization problem is highly non-linear, α_k is iteratively sought with quadratic interpolation (Fujii, 2005). However, in a linear or weakly non-linear problem, such as the one considered here in this study, the initial guess of $\alpha_k = 1$ is valid at most iterations. By the L-BFGS formula, $\tilde{\mathbf{H}}_{k,0}$ is calculated with m pairs of $\tilde{\mathbf{y}}_k (= \tilde{\mathbf{g}}_k - \tilde{\mathbf{g}}_{k-1})$ and $\tilde{\mathbf{p}}_k (= \tilde{\mathbf{x}}_k - \tilde{\mathbf{x}}_{k-1})$ that are derived from the previous iterations as

$$\tilde{\mathbf{H}}_{k,-m} = \gamma_k \mathbf{I}, \tag{5}$$

$$\tilde{\mathbf{H}}_{k,l} = \tilde{\mathbf{V}}_{k+l}^{\mathrm{T}}\tilde{\mathbf{H}}_{k,l-1}\tilde{\mathbf{V}}_{k+l} + \tilde{\rho}_{k+l}\tilde{\mathbf{p}}_{k+l}\tilde{\mathbf{p}}_{k+l}^{\mathrm{T}}, \qquad (l = -m+1, \cdots, -1, 0), \tag{6}$$

where $\mathbf{I}$ is the identity matrix, $\tilde{\rho}_k = 1/\tilde{\mathbf{y}}_k^{\mathrm{T}}\tilde{\mathbf{p}}_k$ and $\tilde{\mathbf{V}}_k = \mathbf{I} - \tilde{\rho}_k\tilde{\mathbf{p}}_k\tilde{\mathbf{y}}_k^{\mathrm{T}}$. γ_k represents the scaling coefficient (Shanno and Phua, 1978) calculated as

$$\gamma_k = \tilde{\mathbf{y}}_k^{\mathrm{T}}\tilde{\mathbf{p}}_k / \tilde{\mathbf{y}}_k^{\mathrm{T}}\tilde{\mathbf{y}}_k. \tag{7}$$

Using non-transformed variables, the above Eqs. (5)-(7) are simply rewritten by replacing $\mathbf{I}$ with $\mathbf{B}$ as

$$\mathbf{H}_{k,-m} = \gamma_k \mathbf{B}, \tag{8}$$

$$\mathbf{H}_{k,l} = \mathbf{V}_{k+l}^{\mathrm{T}}\mathbf{H}_{k,l-1}\mathbf{V}_{k+l} + \rho_{k+l}\mathbf{p}_{k+l}\mathbf{p}_{k+l}^{\mathrm{T}}, \qquad (l = -m+1, \cdots, -1, 0), \tag{9}$$

where $\rho_k = 1/\mathbf{y}_k^{\mathrm{T}}\mathbf{p}_k$ and $\mathbf{V}_k = \mathbf{I} - \rho_k\mathbf{p}_k\mathbf{y}_k^{\mathrm{T}}$, and

$$\gamma_k = \mathbf{y}_k^{\mathrm{T}}\mathbf{p}_k / \mathbf{y}_k^{\mathrm{T}}\mathbf{z}_k, \tag{10}$$

where $\mathbf{z}_k = \mathbf{B}\mathbf{y}_k = \mathbf{h}_k - \mathbf{h}_{k-1}$ and $\mathbf{h}_k = \mathbf{B}\mathbf{g}_k$. Then, the search direction can be expressed as a linear combination of $\mathbf{h}$, $\mathbf{z}$, and $\mathbf{p}$ as

$$\mathbf{d}_k = -\gamma_k\mathbf{h}_k + \sum_{l=-m+1}^{0} \left(a_{k,l}\mathbf{z}_{k+l} + b_{k,l}\mathbf{p}_{k+l} \right), \tag{11}$$

where $a_{k,l}$ and $b_{k,l}$ are the scalar coefficients that are determined by $\mathbf{h}_k$ and m pairs of $\mathbf{p}$ and $\mathbf{z}$ (details are described in Appendix B). It should be noted here that Eq. (11) does not require $\mathbf{B}^{-1}$ calculation. In order to avoid the calculation of $\mathbf{B}^{-1}$, we introduce $\mathbf{c}_k = \mathbf{B}^{-1}\mathbf{x}_k$, $\mathbf{q}_k = \mathbf{B}^{-1}\mathbf{p}_k$, and $K_k = \frac{1}{2}\mathbf{x}_k\mathbf{B}^{-1}\mathbf{x}_k$. The cost function and its gradient at iteration k are written as

$$J(\mathbf{x}_k) = K_k + \frac{1}{2}\left(\mathbf{M}\mathbf{x}_k - \mathbf{y}^{\mathrm{dobs}}\right)^{\mathrm{T}}\mathbf{R}^{-1}\left(\mathbf{M}\mathbf{x}_k - \mathbf{y}^{\mathrm{dobs}}\right), \tag{12}$$

$$\mathbf{g}_k = \mathbf{c}_k + \mathbf{M}^{\mathrm{T}}\mathbf{R}^{-1}\left(\mathbf{M}\mathbf{x}_k - \mathbf{y}^{\mathrm{dobs}}\right). \tag{13}$$

Along with the updating of $\mathbf{x}$ by

$$\mathbf{x}_k = \mathbf{x}_{k-1} + \alpha_k \mathbf{d}_k = \mathbf{x}_{k-1} + \mathbf{p}_k, \tag{14}$$

K_k can ~~be~~ also recursively updated as

$$K_k = K_{k-1} + \mathbf{p}_{k-1}^{\mathrm{T}}\left(\mathbf{c}_{k-1} + \frac{1}{2}\mathbf{q}_{k-1}\right). \tag{15}$$

5 Furthermore, $\mathbf{c}_k$ and $\mathbf{q}_k$ can be updated using Eqs. (14) and (11) respectively as

$$\mathbf{c}_k = \mathbf{c}_{k-1} + \mathbf{q}_{k-1}, \tag{16}$$

$$\mathbf{q}_k = \alpha_k \mathbf{B}^{-1}\mathbf{d}_k = \alpha_k \left(-\gamma_k \mathbf{g}_k + \sum_{l=-m+1}^{0}\left(a_{k,l}\mathbf{y}_{k+l} + b_{k,l}\mathbf{q}_{k+l}\right)\right). \tag{17}$$

In practice, POpULar uses the above equations of (10)–(17) with the initial condition of

$$\mathbf{x}_0 = \mathbf{0}, \tag{18}$$

10 $$K_0 = 0, \tag{19}$$

$$\mathbf{c}_0 = \mathbf{0}, \tag{20}$$

$$\mathbf{g}_0 = \mathbf{M}^{\mathrm{T}}\mathbf{R}^{-1}\left(\mathbf{M}\mathbf{x}_0 - \mathbf{y}^{\mathrm{dobs}}\right), \tag{21}$$

$$\mathbf{h}_0 = \mathbf{B}\mathbf{g}_0, \tag{22}$$

$$\mathbf{d}_0 = -\mathbf{h}_0. \tag{23}$$

15 Thus, we can see that the sequence of these equations do not require $\mathbf{B}^{-1}$. Practical calculations of Eqs. (11) and (17) are described in Appendix B.

2.2 Identical twin experiment design

The identical twin experiment is designed for atmospheric CO_2 inversion. We first run a forward simulation to construct a set of pseudo atmospheric observations using a prescribed flux dataset considered as "true fluxes". In the experiment, a different

20 flux dataset is used as the prior fluxes and the pseudo observations are assimilated into the system to modify the prior fluxes, which is expected to converge to the true flux. The validity of the inversion system can be elucidated by evaluating how close the posterior fluxes have approached the true fluxes after the assimilation.

The analysis period, i.e., assimilation window, is chosen as the year of 2010 and monthly mean CO_2 fluxes are optimized in the inversion. Therefore, the number of control variables to be optimized is 12 (months) $\times$ 10,242 (the number of horizontal

25 grid points) = 122,904. Since we do not optimize the initial concentrations, we use the same initial concentrations for the true and assimilation runs.

2.2.1 True and prior flux datasets

We have prepared a prior flux dataset that will be used in future inversions with real atmospheric observations. But for this study, we have prepared the "true flux" dataset mentioned above, terrestrial fluxes of which are already optimized to some

extent by another inversion and explicitly includes biomass burning data. Table 1 summarizes the prior and true flux datasets. All of the prior and true flux data are provided as monthly mean. As commonly done for prior and true fluxes, we use the fossil fuel emissions of Carbon Dioxide Information Analysis Center (CDIAC) (Andres et al., 2013). Thus, we assume that the fossil fuel emissions in the prior flux dataset is perfectly known and fluxes other than the fossil-fuel emissions are optimized in the inversion.

For terrestrial biosphere and ocean fluxes, the prior flux dataset uses net biome production (NBP) data from a process-based ecosystem model called Vegetation Integrative SImulator for Trace Gases (VISIT: Ito and Inatomi, 2012), and sea-air exchange data based on shipboard ΔpCO_2 measurements calculated by Japan Meteorological Agency (Iida et al., 2015), respectively. For the true flux dataset, we use net ecosystem production (NEP) data of Carnegie-Ames-Stanford-Approach (CASA) model (Randerson et al., 1997) modified by the inversion of Niwa et al. (2012) and climatological ΔpCO_2-based sea-air exchange data of Takahashi et al. (2009). The true flux dataset also contains biomass burning emissions from the Global Fire Emissions Database (GFED) version 3.1 (van der Werf et al., 2010). The reason of the inversion modification of the CASA flux field is that the original CASA NEP is annually balanced (annually integrated flux is zero everywhere). Therefore, we scaled the terrestrial flux values at each latitude band and month so that the zonal average value coincides with a more realistic value of the inversion flux calculated by Niwa et al. (2012). The inversion flux is the average for 2006–2008, in which the global terrestrial biosphere uptake is 4.4 Pg C yr^{-1}. Readers should note that NEP of CASA and NBP of VISIT represent different fluxes; in addition to NEP, NBP has additional sources of biospheric respiration and combustion emissions caused by natural and anthropogenic disturbances. By replacing the original CASA fluxes with the inversion fluxes and adding the biomass burning emissions, both the true and prior land fluxes represent emissions with same sources.

20 **2.2.2 Pseudo observations**

Pseudo observations are constructed from the on-line calculation using NICAM-TM driven by the true flux dataset. After a three-year spin-up, concentration values are extracted at 65 locations that emulate well-known CO_2 ground-based observation sites (locations are shown in Fig. 2 and detail information is listed in Appendix C). Although some sites actually operate *in situ* continuous observations, we assume, for simplicity, that flask air sampling observations are made at all the sites with one-week sampling frequency. Therefore, the total number of observation data is 65 (sites) × 52 (weeks) = 3,380. The timing of flask sampling is set at 13:00 LST at each site for sampling in well-mixed air masses. Random values with a standard deviation of 0.2 ppm are added to the extracted model values to mimic actual measurement uncertainties.

2.2.3 Prior error covariance

Diagonal elements of **B** (variance) are derived from absolute differences between the prior and true fluxes that are scaled for 30 specified global and ocean total values as

$$B_{i,i} = \left(r|x_i^{\text{pri}} - x_i^{\text{true}}| \right)^2, \tag{24}$$

where i denote the element index, and r is the scaling factor. x^{pri} and x^{true} represent the prior and true flux values, respectively, but at this stage we exclude the biomass burnings of GFED from the true fluxes. The scaling factor r is determined so that the annual global uncertainty

$$\sigma = \sqrt{\mathbf{aBa}^{\mathrm{T}}} \tag{25}$$

5   corresponds to $3.0\,\mathrm{Pg\,C\,yr^{-1}}$ and $0.5\,\mathrm{Pg\,C\,yr^{-1}}$ for land and ocean fluxes, respectively. The vector $\mathbf{a}$ acts as the spatiotemporal averaging operator and $\mathbf{ax}$ produces the annual global average of $\mathbf{x}$. In fact, using the difference between $\mathbf{x}^{\mathrm{pri}}$ and $\mathbf{x}^{\mathrm{true}}$ provides some ideal error variance distributions, although $\mathbf{x}^{\mathrm{true}}$ does not include the biomass burnings of GFED. When using real observations, $\mathbf{x}^{\mathrm{true}}$ is of course unknown. Therefore, this ideal error covariance would overestimate the performance of the inversion system. We recognize that the prior variance setting critically influences the optimization quality; however, the task of seeking
10   appropriate variances is out of the scope of this study. Nevertheless, not including the biomass burnings in $\mathbf{x}^{\mathrm{true}}$ would help us to elucidate the ability of the inversion system to find large CO_2 flux anomalies.

For the off-diagonal elements in matrix $\mathbf{B}$, we introduce a simple spatial correlation with the Gaussian function in the off-diagonal elements (covariance) as

$$B_{i,j} = B_{i,i}B_{j,j}\exp\left(-\frac{l_{i,j}^2}{2L^2}\right), \quad i \neq j, \tag{26}$$

15   where $l_{i,j}$ is the horizontal length between i and j and L is the correlation scale length. Here, we assume no temporal correlation since we are optimizing relatively low temporal resolution fluxes (monthly means). In Eq. (26), we use the globally unique scale lengths for land and ocean, L_{lnd} and L_{ocn}, set at 500 km and 1000 km, respectively. There is no cross correlation between land and ocean fluxes. These correlation scale lengths are determined from the results of previous studies (such as Rödenbeck, 2005; Chevallier et al., 2007; Basu et al., 2013), although they did not use the Gaussian function as in Eq. (26) but used instead
20   an exponential decay function. As is the case with the variance, we leave the determination of optimal values for L for a future study. Figure 2 shows four examples of the error correlation distributions determined by $\exp(-l^2/2L^2)$ with $L_{\mathrm{lnd}} = 500$ km and $L_{\mathrm{ocn}} = 1000$ km.

2.2.4 Observation-model misfit error covariance

We set the error covariance for model-observation misfit $\mathbf{R}$ at $1\,\mathrm{ppm}^2$ (ppm is used here as equivalent to the dry air mole fraction
25   unit of μ-mol mol^{-1}) for all the variances and $0\,\mathrm{ppm}^2$ for all the covariances; therefore, $\mathbf{R}$ is a unit diagonal matrix. Actually, introducing off-diagonal elements in $\mathbf{R}$ is difficult compared to $\mathbf{B}$ because the inverse calculation of $\mathbf{R}$ is necessary at some stage in the calculation. Nevertheless, the "no covariance" assumption is relatively reasonable considering the sparse spatiotemporal distribution of the observations used here. The misfit uncertainty of 1 ppm is arbitrary but reasonable in representing model-observation misfits, based on the reported numbers published in previous studies (e.g. Patra et al., 2008).

2.2.5 Diagnostic measures

After the assimilation, we evaluate how close the posterior fluxes approach the true fluxes, by using root-mean-square error (RMSE) measures described below. On the global scale, we use

$$\text{GRMSE} = \sqrt{\frac{1}{N}\frac{1}{12}\sum_{i=1}^{N}\sum_{m=1}^{12}\left(x_{i,m}^{\text{post}} - x_{i,m}^{\text{true}}\right)^2}, \qquad (27)$$

5   where i and m denote the ith model grid and the mth month, respectively, and N denotes the number of model grids. x^{post} represents the posterior flux value and x^{true} denotes the true flux value including the biomass burnings. We also investigate error distributions by

$$\text{RMSE} = \sqrt{\frac{1}{12}\sum_{m=1}^{12}\left(x_{i,m}^{\text{post}} - x_{i,m}^{\text{true}}\right)^2}, \qquad (28)$$

calculated for each model grid i.

10 ## 2.3 Sensitivity tests

Using the above twin experiment, we conducted sensitivity tests to elucidate impacts on the inversion results due to the differences in the adjoint models (discrete or continuous) and optimization schemes.

   As described in Niwa et al. (2016), the linearity of the discrete adjoint is ensured and the perfect adjoint relationship is achieved with the forward model in which the non-linear flux limiter (Thuburn, 1996) in the advection calculation is turned 15 off. On the other hand, the continuous adjoint has the same non-linear flux limiter as that of the forward model calculation to maintain the monotonicity of the advection adjoint. Although this fails to achieve perfect adjoint relationship with the forward model, smaller model transport errors are obtained. Therefore, we have tested two forward and adjoint model sets: one set preserves linearity and complete adjoint relations using the forward model without the flux limiter and the discrete adjoint model (LINEAR), while the other one is a non-linear and non-exact adjoint set using the forward model with the flux limiter 20 and the continuous adjoint model (NON-LINEAR).

   Originally, the POpULar optimization scheme was designed for non-linear problems of ocean dynamics by modifying the linear optimization scheme of DR89, as described above. In atmospheric CO_2 inversion, atmospheric transport process is treated as linear, i.e., tracer is passive, and non-linear chemical process not involved. if we use the NON-LINEAR model set, the problem becomes slightly non-linear due to the use of the flux limiter. Therefore, we also examine 25 the behavior of the linear (DR89) and non-linear (POpULar) optimization schemes with the two model sets (LINEAR and NON-LINEAR).

   Furthermore, we also compare results between the two case with diagonal **B** and with off-diagonal **B**, to confirm the effectivity of prior error correlations. In the diagonal **B** case, we set the off-diagonal elements to zero and rescale the diagonal elements by r (Eq. 24) that the global uncertainty σ (Eq. 25) that of the off-diagonal **B**. In summary, we

conduct eight sensitivity tests using the LINEAR/NON-LINEAR model sets, the DR89 and POpULar optimization schemes and diagonal and off-diagonal **B** (Table 2).

3   Results

3.1   Sensitivities to adjoint models, optimization schemes, and error correlations

5   In each of the sensitivity tests, we perform a total of 60 iterations to optimize the surface fluxes. Figure 3 shows GMRSE variations against the number of iterations and Table 2 lists GRMSE values after 60 iterations. As the iterative calculation proceeds, GRMSE shows smooth reduction in all the cases except for the case of NON-LINEAR+DR89 with the diagonal **B** (Fig. 3a), where GRMSE reduction in value matches that of its corresponding LINEAR case. But after about 30 iterations, the two curves diverge rapidly as the NON-LINEAR case increases in GRMSE to a value at the 60th iteration greater than the value

10   at the beginning of the iteration. This is due to the fact that DR89 is strictly designed for a linear problem (Appendix A) and hence is incompatible with NON-LINEAR. However, if ~~off-diagonal **B** is used~~, NON-LINEAR+DR89 produces a GRMSE reduction curve similar to that of the LINEAR case (Fig. 3c). This may be due to the fact that the smoothing effect of the error correlation in **B** suppresses the incompatibility of DR89 with NON-LINEAR.

~~On the other hand,~~ POpULar does not show such incompatibility with NON-LINEAR (Figs. 3b and d). This is because

15   the POpULar optimization algorithm allows model non-linearity. For the LINEAR cases, the GRMSE values from the use of POpULar are the same as those in the DR89 cases, irrespective of the prior error covariance setting (Table 2).

Although the differences are modest, NON-LINEAR generates smaller GRMSE values than those from LINEAR while using POpULar, which is apparent especially with the off-diagonal **B** (Fig. 3d). This is because of the smaller model error property of the NON-LINEAR model set. In the non-linear case, the cost function defined by Eq. (1) is no longer quadractic

20   and the minimum point is not uniquely determined. Therefore, use of the NON-LINEAR model set has a risk of falling into a local minimum, causing deterioration of the optimization. The result indicates that, for the CO_2 inversion problem considered here, the smaller model error ~~of NON-LINEAR surpasses the negative effect of its non-linearity~~.

Comparing Figs. 3c and d with Figs. 3a and b, we see that the off-diagonal **B** produces significantly smaller GRMSE than the diagonal **B**. The reduction ratio in GRMSE from the prior value (5.59×10^{-7} mol m^{-2} s^{-1}) increases by about 15 %; the

25   GRMSE value reduces from 4.07–4.10×10^{-7} mol m^{-2} s^{-1} (excluding the case of NON-LINEAR+DR89) to 3.21–3.37×10^{-7} mol m^{-2} s^{-1} by introducing the error correlation in **B**. An implication of this result, especially for the global ocean, is that the diagonal **B** fails to reduce GRMSE from the prior condition (Table 2). Intrinsically, the optimization of the ocean fluxes is difficult compared to that of the land fluxes, because ocean flux variations are much smaller than those associated with the land, but also in our case we use true ocean flux that is similar to the prior flux. The result indicates that introducing spatial

30   error correlations in **B** is necessary in order to modify such small ocean fluxes.

Figure 4 shows RMSE distributions of the posterior fluxes calculated with the diagonal and off-diagonal **B**; the RMSE distribution of the prior flux is also shown as a reference. Posterior fluxes are produced after 60 iterations using POpULar+NON-LINEAR. As already indicated in Figs. 3c and d, RMSEs of the two posterior fluxes are much ~~less~~ than that of the prior,

demonstrating the optimization skill of our new system. The prior flux has RMSE ~~much more than~~ 15×10^{-7} mol m^{-2} s^{-1} in the terrestrial areas, where biosphere activity is large (e.g., eastern North America, South America, East and Southeast Asia, and Africa) (Fig. 4d). Those errors are effectively reduced by the assimilation to values mostly less than 10×10^{-7} mol m^{-2} s^{-1}. Moreover, in the off-diagonal **B** case, the errors are further reduced, especially in the areas where observations are sparse,

5 e.g., Africa, South Asia, South America, and Australia (Fig. 4c). This indicates that introducing error correlations allows an effective propagation of atmospheric CO_2 information to surface fluxes located beyond the observation footprints that are determined by atmospheric flow fields.

3.2 Posterior flux features

In this section, we present general features of the posterior fluxes and compare them with the true fluxes. We assess when,

10 where and how much the posterior fluxes are reliable when real observations are used. The posterior fluxes analyzed here are derived after 60 iterations by NON-LINEAR+POpULar with the off-diagonal **B**, which has been shown to display the smallest error among the above eight sensitivity tests.

First, we compare atmospheric CO_2 concentration fields that are generated by the forward NICAM-TM from the true, prior and posterior fluxes. Figure 5a shows the time series of simulated atmospheric concentrations at the Minamitorishima (MNM)

15 observation site, located on western North Pacific. In fact, the pseudo observation network (Appendix C) includes MNM and its location is shown in Fig. 2. In Fig. 5a, we see a good agreement between the posterior and the observational concentration values. The root mean square difference between them is 0.19 ppm, which is much less than the prescribed model-observation misfit error ~~of 1 ppm (Section 2.2.4)~~. This follows from the fact that we have perfect transport simulation. That is, the same transport model is used for preparing the observations and the assimilation. The prescribed value of 1 ppm is rather inflated

20 (but reasonable for a practical inversion with real observations), but it is expected that the difference between the posterior and observed concentration is close to the random error of 0.2 ppm that we add to the observations (Section).

Figures 5b-d show latitude-time cross sections of zonally averaged surface concentration simulated from the true, prior and posterior fluxes. Compared to the concentration field generated from the true fluxes, a period of low concentration at the northern latitudes starts one month earlier in the field forced by the prior fluxes. Furthermore, latitudinal gradients between

25 30°S and 30°N are weaker during January–May. These features are modified by the assimilation so that the spatiotemporal variation of the posterior CO_2 concentration is nearly identical to the ~~one~~ obtained from the true flux (Fig. 5d).

To see the degree of similarity in the flux distribution between the posterior and true fluxes, we show monthly mean flux distribution for March, July and September of 2010 in Fig. 6, along with the corresponding prior fluxes. As shown in Fig. 6, the general pattern of the true flux for each month is retrieved relatively well, as indicated in the posterior flux distribution,

30 from the prior flux.

For March, the true flux has larger sources in the northern mid- to high-latitudes than those of the prior flux and this feature is retrieved well by the inversion (Figs. 6a-c). Furthermore, it is noteworthy that the inversion successfully retrieves the distinct source/sink contrast patterns around the equator in Africa and South America. For July, the true flux shows a larger biosphere sink in the northern latitudes than ~~the one captured by~~ the prior flux; the posterior flux calculated by our inversion method shows

a sink of similar magnitude as ~~detected in~~ the true flux (Figs. 6d-f). However, there ~~is~~ a mismatch in the spatial distribution of the sink. Upon closer ~~look,~~ one can see that the posterior flux has large sinks in West Siberia and eastern North America (Fig. 6e), while the true flux has a comparably large sink in western Canada (Fig. 6f). During the summer season, vertical transport over a continental region is quite active, and the emission from the surface ~~becomes~~ well mixed in the vertical. Therefore,

5   ground-based stations observe only diluted flux signals, resulting in weak constraint on the flux estimation. For September, the prior flux is still characterized by sinks over most of the continental regions. However, the true flux has already changed to a source in northern high-latitudes, and the posterior flux is able to reproduce that feature (Figs. 6g-i). Moreover, the distinct source/sink contrasts in Africa and South America, signs of which are opposite to those in March, are again well retrieved by the inversion. The ideal prior error variance (Section 2.2.3) might have helped this achievement to some extent. Using

10   differences between the true and prior fluxes to determine the prior error variance allows the system to know where and by how much observational signals should propagate to surface fluxes. But it is not able to assign the sign of the flux (source or sink), only the magnitude. Therefore, these results suggest that our new inversion system is capable of reproducing continental flux patterns from surface observations only.

Furthermore, the inversion is able to detect successfully "hot spot"-like CO_2 sources from biomass burnings. In Fig. 7, we

15   focus on the fluxes in Indochina for March, and in South America and Africa for September of 2010. In those regions, the true fluxes derived from GFED show regional anomalies. In 2010, large biomass burnings occurred under a severe dry condition in Amazon (Lewis et al., 2011). Compared to the prior fluxes that have moderate spatial variations, the posterior fluxes show large sources in those areas that are comparable to the true flux patterns, though the posterior source peaks are underestimated in Thailand and Amazon, and are shifted from the coast to the inland area in southern Africa. It should be noted that in this

20   exercise, we do not use biomass burning information to assign the prior error variance (Section 2.2.3). Therefore, these results suggest that our new inversion system is capable of detecting even regionally limited flux anomalies. Such capability will be enhanced if more observations are available.

Figure 8 compares zonally-integrated seasonal cycles of the posterior fluxes over terrestrial and ocean areas in three latitudinal bands with those of the prior and true fluxes. As expected from Fig. 6, the seasonal cycle of the posterior flux agrees

25   generally well with that of the true flux, compared to that of the prior flux. However, the degree of agreement is latitudinally dependent. The region where the amplitude and the phase of the seasonal cycle of the posterior flux agree the most with those of the true flux is in the northern mid- to high-latitude band (30–90°N) (Figs. 8a and b), for both the land and the ocean. The result reflects the ~~existence of~~ relatively dense surface observation network in this latitude zone. The seasonal cycles of the posterior fluxes in the other latitudinal bands (30°S–30°N and 30–90°S) show moderate similarities to the true flux seasonal cycles. The

30   largest difference can be seen for the ocean flux in the 30–90°S latitude band, particularly during the southern hemisphere fall season. Improvements could be made, but the seasonal amplitudes are very small and are difficult to ~~be~~ retrieve~~d~~.

Latitudinal profiles of annual zonal mean fluxes can also be retrieved well (Fig. 9). For example, compared to the prior flux, the posterior flux matches the true flux and shifts the sink towards lower latitudes (Fig. 9a). Moreover, the true and posterior fluxes consistently show two distinct source peaks across the equator. Figure 9b shows that this flux pattern is due mostly to the

35   terrestrial flux (Fig. 9b). In the southern extra tropics, on the other hand, the posterior flux is not modified significantly from the

prior flux, suggesting weak constraints due to a sparse number of observational stations in that area. Compared to the terrestrial flux, the ocean flux has much smaller latitudinal variations (Fig. 9c). In spite of such small variations, we see improvements in the prior flux by the inversion in the northern latitudinal band of 30–60°N and in the Southern Ocean in the latitudinal band of 50–70°S. At other latitudes, the posterior flux has similar profiles to those of the prior flux.

4 Conclusions

In this paper, we have introduced, described and tested our new 4D-Var inversion system based on the icosahedral grid model, NICAM. Adding to the off-line forward and adjoint models of NICAM-TM, this study has introduced the optimization method of POpULar, which constitutes an essential part of the 4D-Var system. Moreover, we have conducted identical twin experiments to confirm the capability and utility of the new system for atmospheric CO_2 inversion.

Based on the results of the sensitivity tests using various combinations of the optimization method (DR89 and POpULar) and the discrete and continuous adjoint models (LINEAR and NON-LINEAR), we have found that a combination of POpULar and the continuous adjoint (NON-LINEAR+POpULar) has produced the least error. This is due to the less transport error of the continuous adjoint and the flexibility of the POpULar optimization method against the model non-linearity. Even with the discrete adjoint, POpULar shows high optimization capability, but its error is slightly larger than when used with the continuous adjoint. Therefore, if model linearity and perfect adjoint relationship are strongly required, the combination of LINEAR+POpULar could be another choice.

We have introduced spatial error correlations in the off-diagonal elements of the prior error covariance and have shown that it significantly improves the posterior fluxes, reducing the global flux error by about 15 %. This result is consistent with other 4D-Var inversions, but we have achieved it an easier way that does not require matrix inverse calculation nor any matrix decomposition; the optimization algorithm of POpULar has an advantage in its simple treatment of the off-diagonal matrix. This would prove to be a more powerful tool when more complicated flux error structures are considered. For instance, Meirink et al. (2008) assumed that the spatial and temporal correlations are mutually independent, but POpULar would enable us to consider cross correlations in space and time. In this study, arbitrary numbers and an ideal prior errors have been used respectively for the error correlation scales and the diagonal elements (variance) of the prior error covariance matrix. Therefore, our next stage of research will involve an investigation of optimal prior error design, taking the advantage of POpULar.

By using our new 4D-Var inverse system, we have successfully retrieved general features of the true flux variations from weekly flask observations obtained from 65 ground-based stations. Moreover, a remarkable performance of the new system is demonstrated by the result that the inversion is able to detect regionally limited flux anomalies caused by biomass burnings. However, even with the perfect (non-biased) transport model and the ideal prior error variances, improvements in the prior flux estimate in some regions have been found to be limited due to the sparseness of the observations. Further improvements are expected by adding data from *in situ* continuous measurements and worldwide observations by aircraft (e.g. Machida et al., 2008) and satellites (e.g. Yoshida et al., 2013; Saitoh et al., 2016) in a future study.

Code availability

Development of NICAM-TM 4D-Var and experimental studies of its application are being continued by the authors. The source codes of NICAM-TM 4D-Var are available for those who are interested. The source codes of NICAM-TM are included in the package of the parent model NICAM, which can be obtained upon request under the general terms and conditions
5 (http://nicam.jp/hiki/?Research+Collaborations). The source code of POpULar is also accessible by contacting Yosuke Fujii of Meteorological Research Institute (http://www.mri-jma.go.jp/Member/oc/kefujiiyosukefu_en.html).

Appendix A: Optimization scheme of Derber and Rosati (1989)

The conjugate gradient method with the preconditioning of $\tilde{\mathbf{x}} = \mathbf{B}^{-1/2}\mathbf{x}$ uses the following equations:

$$\tilde{\mathbf{x}}_k = \tilde{\mathbf{x}}_{k-1} + \alpha_k \tilde{\mathbf{d}}_{k-1}, \tag{A1}$$

10 $$\beta_k = \tilde{\mathbf{g}}_k^{\mathrm{T}} \tilde{\mathbf{y}}_k / \tilde{\mathbf{d}}_{k-1}^{\mathrm{T}} \tilde{\mathbf{y}}_k, \tag{A2}$$

$$\tilde{\mathbf{d}}_k = -\tilde{\mathbf{g}}_k + \beta_k \tilde{\mathbf{d}}_{k-1}. \tag{A3}$$

With the non-transformed variables, the above equations can be rewritten as

$$\mathbf{x}_k = \mathbf{x}_{k-1} + \alpha_k \mathbf{d}_{k-1}, \tag{A4}$$

$$\beta_k = \mathbf{h}_k^{\mathrm{T}} \mathbf{y}_k / \mathbf{d}_{k-1}^{\mathrm{T}} \mathbf{y}_k, \tag{A5}$$

15 $$\mathbf{d}_k = -\mathbf{h}_k + \beta_k \mathbf{d}_{k-1}. \tag{A6}$$

Here we should note that $\mathbf{B}^{-1}$ nor $\mathbf{B}^{1/2}$ is not required, but only the multiplication $\mathbf{h}_k = \mathbf{B}\mathbf{g}_k$ is calculated. If a linear problem is considered, Eq. (A5) is written as

$$\beta_k = \mathbf{h}_k^{\mathrm{T}} \mathbf{g}_k / \mathbf{h}_{k-1}^{\mathrm{T}} \mathbf{g}_{k-1}, \tag{A7}$$

and this is used in DR89. Introducing $\mathbf{e} = \mathbf{B}^{-1}\mathbf{d}$, the step length α_k is calculated as

20 $$\mathbf{f}_k = \mathbf{e}_{k-1} + \mathbf{M}^{\mathrm{T}}\mathbf{R}^{-1}\mathbf{M}\mathbf{d}_{k-1}, \tag{A8}$$

$$\alpha_k = -\mathbf{g}_{k-1}^{\mathrm{T}} \mathbf{d}_{k-1} / \mathbf{d}_{k-1}^{\mathrm{T}} \mathbf{f}_k. \tag{A9}$$

Differently from POpULar, Eq. (A9) gives the analytical solution of α_k. If the cost function J is convex quadratic, i.e., linear problem, α_k can be derived analytically by

$$\alpha_k = -\mathbf{g}_{k-1}^{\mathrm{T}} \mathbf{d}_{k-1} / \left(\mathbf{d}_{k-1}^{\mathrm{T}} \mathbf{Q} \mathbf{d}_{k-1} \right), \tag{A10}$$

25 where $\mathbf{Q}$ is the Hessian of J ($= \mathbf{B}^{-1} + \mathbf{M}^{\mathrm{T}}\mathbf{R}^{-1}\mathbf{M}$) (Nocedal and Wright, 2006). One may easily find the above equation is the same as Eq. (A9). Such an analytical calculation of α_k is the so-called exact line search. After the updates of $\mathbf{x}$ with Eq. (A4)

and $\mathbf{d}$ with Eq. (A6), $\mathbf{g}$ and $\mathbf{e}$ are updated as

$$\mathbf{g}_k = \mathbf{g}_{k-1} + \alpha_k \mathbf{f}_k, \tag{A11}$$

$$\mathbf{e}_k = -\mathbf{g}_k + \beta_k \mathbf{e}_{k-1}. \tag{A12}$$

Starting from the initial condition of

$$\mathbf{x}_0 = \mathbf{0}, \tag{A13}$$

$$\mathbf{g}_0 = \mathbf{M}^\mathrm{T} \mathbf{R}^{-1} \mathbf{d}^{\mathrm{dobs}}, \tag{A14}$$

$$\mathbf{h}_0 = \mathbf{B} \mathbf{g}_0, \tag{A15}$$

$$\mathbf{d}_0 = -\mathbf{h}_0, \tag{A16}$$

$$\mathbf{e}_0 = -\mathbf{g}_0, \tag{A17}$$

equations (A4)–(A12) are repeatedly calculated until the values of $\mathbf{x}$ are converged ~~enough.~~

Appendix B: Practical calculations of d and q

Practical derivations of $\mathbf{d}_k$ and $\mathbf{q}_k$ (Eqs 11 and 17) are as follows:

$$\mathbf{s}_0 = -\mathbf{h}_k, \tag{B1}$$

$$\mathbf{t}_0 = -\mathbf{g}_k, \tag{B2}$$

$$\mathbf{s}_{l-1} = \mathbf{s}_l - \rho_{k+l} \mathbf{t}_l^\mathrm{T} \mathbf{p}_{k+l} \mathbf{z}_{k+l} \quad (l = 0, -1, \cdots, -m+1), \tag{B3}$$

$$\mathbf{t}_{l-1} = \mathbf{t}_l - \rho_{k+l} \mathbf{t}_l^\mathrm{T} \mathbf{p}_{k+l} \mathbf{y}_{k+l} \quad (l = 0, -1, \cdots, -m+1), \tag{B4}$$

$$\mathbf{s}'_{-m} = \gamma_k \mathbf{s}_{-m}, \tag{B5}$$

$$\mathbf{t}'_{-m} = \gamma_k \mathbf{t}_{-m}, \tag{B6}$$

$$\mathbf{s}'_l = \mathbf{s}'_{l-1} - \rho_{k+l} \left(\mathbf{t}_l^\mathrm{T} \mathbf{p}_{k+l} - \mathbf{s}'^\mathrm{T}_{l-1} \mathbf{y}_{k+l} \right) \mathbf{p}_{k+l} \quad (l = -m+1, -m+2, \cdots, 0), \tag{B7}$$

$$\mathbf{t}'_l = \mathbf{t}'_{l-1} - \rho_{k+l} \left(\mathbf{t}_l^\mathrm{T} \mathbf{p}_{k+l} - \mathbf{s}'^\mathrm{T}_{l-1} \mathbf{y}_{k+l} \right) \mathbf{q}_{k+l} \quad (l = -m+1, -m+2, \cdots, 0), \tag{B8}$$

$$\mathbf{d}_k = \mathbf{s}'_0, \tag{B9}$$

$$\mathbf{q}_k = \alpha_k \mathbf{t}'_0. \tag{B10}$$

Appendix C: Pseudo observation sites

Table C.1. List of pseudo observation sites used in the identical twin experiment

Site name	Latitude [deg.]	Longitude [deg.]	Altitude [m]
Alert	82.45	-62.51	205
Ny-Alesund	78.91	11.89	479
Mould Bay	76.25	-119.35	35
Summit	72.60	-38.42	3214
Barrow	71.32	-156.61	16
Pallas-Sammaltunturi	67.97	24.12	565
Ocean Station M	66.00	2.00	0
Storhofdi	63.40	-20.29	127
Churchill	58.75	-94.01	35
Baltic Sea	55.35	17.22	28
Cold Bay	55.21	-162.72	57
Mace Head	53.33	-9.90	26
Shemya Island	52.71	174.13	28
Ile Grande	48.80	-3.58	15
Hohenpeissenberg	47.80	11.02	941
Ulaan Uul	44.45	111.10	1012
Black Sea	44.18	28.66	5
Plateau Assy	43.25	77.88	2524
Cape Ochi-ishi	43.15	145.50	50
Begur	41.97	3.23	16
Centro de Investigacion de la Baja Atmosfera	41.81	-4.93	850
Niwot Ridge	40.05	-105.59	3526
Wendover	39.90	-113.72	1332
Point Arena	38.95	-123.74	22
Terceira Island	38.77	-27.38	24
Tae-ahn Peninsula	36.74	126.13	21
Mt. Waliguan	36.29	100.90	3815

Table C.1. (continued)

Site name	Latitude [deg.]	Longitude [deg.]	Altitude [m]
Lampedusa	35.52	12.62	50
Finokalia	35.34	25.67	155
La Jolla	32.90	-117.30	15
Tudor Hill	32.26	-64.88	35
WIS Station	30.86	34.78	482
Izana	28.31	-16.50	2377
Sand Island	28.21	-177.38	15
Key Biscayne	25.67	-80.16	6
Yonagunijima	24.47	123.02	50
Minamitorishima	24.28	153.98	28
Assekrem	23.26	5.63	2715
Mauna Loa	19.54	-155.58	3402
Cape Kumukahi	19.52	-154.82	8
High Altitude Global Climate Observation Center	18.98	-97.31	4469
Cape Rama	15.08	73.83	65
Mariana Islands	13.39	144.66	5
Ragged Point	13.16	-59.43	20
Christmas Island	1.70	-157.15	5
Mt. Kenya	-0.06	37.30	3649
Mahe Island	-4.68	55.53	6
Ascension Island	-7.97	-14.40	90
Arembepe	-12.77	-38.17	6
Tutuila	-14.25	-170.56	47
Cape Ferguson	-19.28	147.06	7
Easter Island	-27.16	-109.43	69
Cape Point	-34.35	18.49	260
Cape Grim	-40.68	144.69	164
Baring Head Station	-41.41	174.87	85
Crozet Island	-46.43	51.85	202
Macquarie Island	-54.48	158.97	11
Tierra Del Fuego	-54.85	-68.31	17
Drake Passage	-59.00	-64.69	5

Table C.1. (continued)

Site name	Latitude [deg.]	Longitude [deg.]	Altitude [m]
Palmer Station	-64.92	-64.00	15
Casey	-66.28	110.52	52
Mawson Station	-67.62	62.87	37
Syowa Station	-69.00	39.58	3
Halley Station	-75.61	-26.21	33
South Pole	-89.98	-24.80	2815

Acknowledgements. We thank Kaz Higuchi of York University, Canada, for his fruitful comments on the manuscript. This study is supported mainly by the Environment Research and Technology Development Fund (2-1401) of the Ministry of the Environment, Japan. This study is also supported partly by the cooperative research for climate system of Atmosphere and Ocean Research Institute, the University of Tokyo, and by "advancement of meteorological and global environmental predictions utilizing observational 'Big Data'" of the social and
5 scientific priority issues (Theme 4) to be tackled by using post K computer of the FLAGSHIP2020 Project. The calculations of this study were performed on the super computer system, FUJITSU PRIMEHPC FX100, of Meteorological Research Institute.

References

Andres, R. J., Boden, T., and Marland, G.: Monthly Fossil-Fuel CO_2 Emissions: Mass of Emissions Gridded by One Degree Latitude by One Degree Longitude, Carbon Dioxide Information Analysis Center, Oak Ridge National Laboratory, U.S. Department of Energy, Oak Ridge, Tenn., U.S.A., doi:10.3334/CDIAC/ffe.MonthlyMass.2013, 2013.

5 Andrews, A. E., Kofler, J. D., Trudeau, M. E., Williams, J. C., Neff, D. H., Masarie, K. A., Chao, D. Y., Kitzis, D. R., Novelli, P. C., Zhao, C. L., Dlugokencky, E. J., Lang, P. M., Crotwell, M. J., Fischer, M. L., Parker, M. J., Lee, J. T., Baumann, D. D., Desai, A. R., Stanier, C. O., Wekker, S. F. J. D., Wolfe, D. E., Munger, J. W., and Tans, P. P.: CO_2, CO, and CH_4 measurements from tall towers in the NOAA Earth System Research Laboratory's Global Greenhouse Gas Reference Network: instrumentation, uncertainty analysis, and recommendations for future high-accuracy greenhouse gas monitoring efforts, Atoms. Meas. Tech., 7, 647–687, doi:10.5194/amt-7-647-2014, 2014.

10 Baker, D. F., Doney, S. C., and Schimel, D. S.: Variational data assimilation for atmospheric CO_2, Tellus, 58B, 359–365, doi:10.1111/j.1600-0889.2006.00218.x, 2006a.

Baker, D. F., Law, R. M., Gurney, K. R., Rayner, P., Peylin, P., Denning, A. S., Bousquet, P., Bruhwiler, L., Chen, Y., Ciais, P., Fung, I. Y., Heimann, M., John, J., Maki, T., Maksyutov, S., Masarie, K., Prather, M., Pak, B., Taguchi, S., and Zhu, Z.: TransCom 3 inversion intercomparison: Impact of transport model errors on the interannual variability of regional CO_2 fluxes, 1988–2003, Global Biogeochem.

15 Cycles, 20, doi:10.1029/2004GB002439, 2006b.

Basu, S., Guerlet, S., Butz, A., Houweling, S., Hasekamp, O., Aben, I., Krummel, P., Steele, P., Langenfelds, R., Torn, M., Biraud, S., Stephens, B., Andrews, A., and Worthy, D.: Global CO_2 fluxes estimated from GOSAT retrievals of total column CO_2, Atoms. Chem. Phys., 13, 8695–8717, doi:10.5194/acp-13-8695-2013, 2013.

Bergamaschi, P., Houweling, S., Segers, A., Krol, M., Frankenberg, C., Scheepmaker, R. A., Dlugokencky, E., Wofsy, S. C., Kort, E. A.,

20 Sweeney, C., Schuck, T., Brenninkmeijer, C., Chen, H., Beck, V., and Gerbig, C.: Atmospheric CH_4 in the first decade of the 21st century: Inverse modeling analysis using SCIAMACHY satellite retrievals and NOAA surface measurements, J. Geophys. Res., 118, 7350–7369, doi:10.1002/jgrd.50480, 2013.

Chevallier, F., Fisher, M., Peylin, P., Serrar, S., Bousquet, P., Bréon, F.-M., Chédin, A., and Ciais, P.: Inferring CO_2 sources and sinks from satellite observations: Method and application to TOVS data, J. Geophys. Res., 110, doi:10.1029/2005JD006390, 2005.

25 Chevallier, F., Bréon, F.-M., and Rayner, P. J.: Contribution of the Orbiting Carbon Observatory to the estimation of CO_2 sources and sinks: Theoretical study in a variational data assimilation framework, J. Geophys. Res., 112, doi:10.1029/2006JD007375, 2007.

Chevallier, F., Wang, T., Ciais, P., Maignan, F., Bocquet, M., Altaf Arain, M., Cescatti, A., Chen, J., Dolman, A. J., Law, B. E., Margolis, H. A., Montagnani, L., and Moors, E. J.: What eddy-covariance measurements tell us about prior land flux errors in CO_2-flux inversion schemes, Global Biogeochem. Cycles, 26, doi:10.1029/2010GB003974, 2012.

30 Conway, T. J., Tans, P. P., Waterman, L. S., Thoning, K. W., Kitzis, D. R., Masarie, K. A., and Zhang, N.: Evidence for interannual variability of the carbon cycle from the National Oceanic and Atmospheric Administration/Climate Monitoring and Diagnostics Laboratory Global Air Sampling Network, J. Geophys. Res., 99, 22 831–22 855, doi:10.1029/94JD01951, 1994.

Derber, J. and Rosati, A.: A Global Oceanic Data Assimilation System, J. Phys. Oceanogr., 19, 1333–1347, 1989.

Enting, I. G.: Inverse Problems in Atmospheric Constituent Transport, Cambridge University Press, New York, 2002.

35 Fujii, Y.: Preconditioned Optimizing Utility for Large-dimensional analyses (POpULar), J. Oceanogr., 61, 167–181, doi:10.1007/s10872-005-0029-z, 2005.

Fujii, Y. and Kamachi, M.: A nonlinear preconditioned quasi-Newton method without inversion of a first-guess covariance matrix in variational analyses, Tellus A, 55, 450–454, doi:10.1034/j.1600-0870.2003.00030.x, 2003.

Gou, T. and Sandu, A.: Continuous versus discrete advection adjoints in chemical data assimilation with CMAQ, Atmos. Environ., 45, 4868–4881, doi:10.1016/j.atmosenv.2011.06.015, 2011.

5   Gurney, K. R., Law, R. M., Denning, A. S., Rayner, P. J., Baker, D., Bousquet, P., Bruhwiler, L., Chen, Y.-H., Ciais, P., Fan, S., Fung, I. Y., Gloor, M., Heimann, M., Higuchi, K., John, J., Maki, T., Maksyutov, S., Masarie, K., Peylin, P., Prather, M., Pak, B. C., Randerson, J., Sarmiento, J., Taguchi, S., Takahashi, T., and Yuen, C.-W.: Towards robust regional estimates of CO_2 sources and sinks using atmospheric transport models, Nature, 415, 626–630, doi:10.1038/415626a, 2002.

Hooghiemstra, P. B., Krol, M. C., Bergamaschi, P., Laat, A. T. J., Werf, G. R., Novelli, P. C., Deeter, M. N., Aben, I., and Röck-
10   mann, T.: Comparing optimized CO emission estimates using MOPITT or NOAA surface network observations, J. Geophys. Res., 117, doi:10.1029/2011JD017043, 2012.

Iida, Y., Kojima, A., Takatani, Y., Nakano, T., Sugimoto, H., Midorikawa, T., and Ishii, M.: Trends in pCO_2 and sea–air CO_2 flux over the global open oceans for the last two decades, J. Oceanogr., 71, doi:10.1007/s10872-015-0306-4, 2015.

Ito, A. and Inatomi, M.: Use of a process-based model for assessing the methane budgets of global terrestrial ecosystems and evaluation of
15   uncertainty, Biogeosciences, 9, 759–773, doi:10.5194/bg-9-759-2012, 2012.

Kopacz, M., Jacob, D. J., Fisher, J. A., Logan, J. A., Zhang, L., Megretskaia, I. A., Yantosca, R. M., Singh, K., Henze, D. K., Burrows, J. P., Buchwitz, M., Khlystova, I., McMillan, W. W., Gille, J. C., Edwards, D. P., Eldering, A., Thouret, V., and Nedelec, P.: Global estimates of CO sources with high resolution by adjoint inversion of multiple satellite datasets (MOPITT, AIRS, SCIAMACHY, TES), Atoms. Chem. Phys., 10, 855–876, doi:10.5194/acp-10-855-2010, 2010.

20   Law, R. M., Peters, W., Rödenbeck, C., Aulagnier, C., Baker, I., Bergmann, D. J., Bousquet, P., Brandt, J., Bruhwiler, L., Cameron-Smith, P. J., Christensen, J. H., Delage, F., Denning, A. S., Fan, S., Geels, C., Houweling, S., Imasu, R., Karstens, U., Kawa, S. R., Kleist, J., Krol, M. C., Lin, S.-J., Lokupitiya, R., Maki, T., Maksyutov, S., Niwa, Y., Onishi, R., Parazoo, N., Patra, P. K., Pieterse, G., Rivier, L., Satoh, M., Serrar, S., Taguchi, S., Takigawa, M., Vautard, R., Vermeulen, A. T., and Zhu, Z.: TransCom model simulations of hourly atmospheric CO_2: Experimental overview and diurnal cycle results for 2002, Global Biogeochem. Cycles, 22, doi:10.1029/2007GB003050, 2008.

25   Lewis, S. L., Brando, P. M., Phillips, O. L., van der Heijden, G. M. F., and Nepstad, D.: The 2010 Amazon Drought, Science, 331, 554–554, doi:10.1126/science.1200807, 2011.

Liu, D. C. and Nocedal, J.: On the limited memory BFGS method for large scale optimization, Mathematical Programming, 45, 503–528, doi:10.1007/BF01589116, 1989.

Liu, J., Bowman, K., Lee, M., Henze, D., Bousserez, N., Brix, H., Collatz, G. J., Menemenlis, D., Ott, L., Pawson, S., Jones, D., and Nassar,
30   R.: Carbon monitoring system flux estimation and attribution: impact of ACOS-GOSAT XCO_2 sampling on the inference of terrestrial biospheric sources and sinks, Tellus B, 66, doi:10.3402/tellusb.v66.22486, 2014.

Lorenc, A. C.: Optimal nonlinear objective analysis, Quart. J. Roy. Meteor. Soc., 114, 205–240, doi:10.1002/qj.49711447911, 1988.

Machida, T., Matsueda, H., Sawa, Y., Nakagawa, Y., Hirotani, K., Kondo, N., Goto, K., Nakazawa, T., Ishikawa, K., and Ogawa, T.: Worldwide Measurements of Atmospheric CO_2 and Other Trace Gas Species Using Commercial Airlines, J. Atmos. Oceanic Technol., 25,
35   1744–1754, doi:10.1175/2008JTECHA1082.1, 2008.

Matsueda, H., Machida, T., Sawa, Y., and Niwa, Y.: Long-term change of CO_2 latitudinal distribution in the upper troposphere, Geophys. Res. Lett., 42, 2508–2514, doi:10.1002/2014GL062768, 2015.

Meirink, J. F., Bergamaschi, P., Frankenberg, C., d'Amelio, M. T. S., Dlugokencky, E. J., Gatti, L. V., Houweling, S., Miller, J. B., Röckmann, T., Villani, M. G., and Krol, M. C.: Four-dimensional variational data assimilation for inverse modeling of atmospheric methane emissions: Analysis of SCIAMACHY observation, J. Geophys. Res., 113, doi:10.1029/2007JD009740, 2008.

Niwa, Y., Patra, P. K., Sawa, Y., Machida, T., Matsueda, H., Belikov, D., Maki, T., Ikegami, M., Imasu, R., Maksyutov, S., Oda, T., Satoh, M., and Takigawa, M.: Three-dimensional variations of atmospheric CO_2: aircraft measurements and multi-transport model simulations, Atoms. Chem. Phys., 11, 13 359–13 375, doi:10.5194/acp-11-13359-2011, 2011a.

Niwa, Y., Tomita, H., Satoh, M., and Imasu, R.: A Three-Dimensional Icosahedral Grid Advection Scheme Preserving Monotonicity and Consistency with Continuity for Atmospheric Tracer Transport, J. Meteor. Soc. Japan, 89, 255–268, doi:10.2151/jmsj.2011-306, 2011b.

Niwa, Y., Machida, T., Sawa, Y., Matsueda, H., Schuck, T. J., Brenninkmeijer, C. A. M., Imasu, R., and Satoh, M.: Imposing strong constraints on tropical terrestrial CO_2 fluxes using passenger aircraft based measurements, J. Geophys. Res., 117, doi:10.1029/2012JD017474, 2012.

Niwa, Y., Hirofumi, T., Satoh, M., Imasu, R., Sawa, Y., Tsuboi, K., Matsueda, H., Machida, T., Sasakawa, M., Belan, B., and Saigusa, N.: A 4D-Var inversion system based on an icosahedral grid model (NICAM-TM 4D-Var v1.0): 1. Off-line forward and adjoint transport models, manuscript submitted for publication, 2016.

Nocedal, J.: Updating quasi-Newton matrices with limited storage, Mathematics of Computation, 35, 773–782, doi:10.1090/S0025-5718-1980-0572855-7, 1980.

Nocedal, J. and Wright, S. J.: Numerical Optimization (2nd edn), Springer, New York, 2006.

Onogi, K., Tsutsui, J., Koide, H., Sakamoto, M., Kobayashi, S., Hatsushika, H., Matsumoto, T., Yamazaki, N., Kamahori, H., Takahashi, K., Kadokura, S., Wada, K., Kato, K., Oyama, R., Ose, T., Mannoji, N., and Taira, R.: The JRA-25 Reanalysis, J. Meteor. Soc. Japan, 85, 369–432, doi:10.2151/jmsj.85.369, 2007.

Patra, P. K., Law, R. M., Peters, W., Rödenbeck, C., Takigawa, M., Aulagnier, C., Baker, I., Bergmann, D. J., Bousquet, P., Brandt, J., Bruhwiler, L., Cameron-Smith, P. J., Christensen, J. H., Delage, F., Denning, A. S., Fan, S., Geels, C., Houweling, S., Imasu, R., Karstens, U., Kawa, S. R., Kleist, J., Krol, M. C., Lin, S.-J., Lokupitiya, R., Maki, T., Maksyutov, S., Niwa, Y., Onishi, R., Parazoo, N., Pieterse, G., Rivier, L., Satoh, M., Serrar, S., Taguchi, S., Vautard, R., Vermeulen, A. T., and Zhu, Z.: TransCom model simulations of hourly atmospheric CO_2: Analysis of synoptic-scale variations of the period 2002-2003, Global Biogeochem. Cycles, 22, doi:10.1029/2007GB003081, 2008.

Peylin, P., Law, R. M., Gurney, K. R., Chevallier, F., Jacobson, A. R., Maki, T., Niwa, Y., Patra, P. K., Peters, W., Rayner, P. J., Rödenbeck, C., van der Laan-Luijkx, I. T., and Zhang, X.: Global atmospheric carbon budget: results from an ensemble of atmospheric CO_2 inversions, Biogeosciences, 10, 6699–6720, doi:10.5194/bg-10-6699-2013, 2013.

Randerson, J. T., Thompson, M. V., Conway, T. J., Fung, I. Y., and Field, C. B.: The contribution of terrestrial sources and sinks to trends in the seasonal cycle of atmospheric carbon dioxide, Global Biogeochem. Cycles, 11, 535–560, doi:10.1029/97GB02268, 1997.

Rayner, P. J., Enting, I. G., Francey, R. J., and Langenfelds, R.: Reconstructing the recent carbon cycle from atmospheric CO_2, $\delta 13C$ and O_2/N_2 observations, Tellus B, 51, 213–232, doi:10.1034/j.1600-0889.1999.t01-1-00008.x, 1999.

Rödenbeck, C.: Estimating CO_2 sources and sinks from atmospheric mixing ratio measurements using a global inversion of atmospheric transport, Max-Planck-Institut für Biogeochemie: Technical Paper 6, 2005.

Saitoh, N., Kimoto, S., Sugimura, R., Imasu, R., Kawakami, S., Shiomi, K., Kuze, A., Machida, T., Sawa, Y., and Matsueda, H.: Algorithm update of the GOSAT/TANSO-FTS thermal infrared CO_2 product (version 1) and validation of the UTLS CO_2 data using CONTRAIL measurements, Atmospheric Measurement Techniques, 9, 2119–2134, doi:10.5194/amt-9-2119-2016, 2016.

Sasakawa, M., Shimoyama, K., Machida, T., Tsuda, N., Suto, H., Arshinov, M., Davydov, D., Fofonov, A., Krasnov, O., Saeki, T., Koyama, Y., and Maksyutov, S.: Continuous measurements of methane from a tower network over Siberia, Tellus B, 62, 403–416, doi:10.1111/j.1600-0889.2010.00494.x, 2010.

Satoh, M., Matsuno, T., Tomita, H., Miura, H., Nasuno, T., and Iga, S.: Nonhydrostatic icosahedral atmospheric model (NICAM) for global cloud resolving simulations, J. Comput. Phys., 227, 3486–3514, doi:10.1016/j.jcp.2007.02.006, 2008.

Satoh, M., Tomita, H., Yashiro, H., Miura, H., Kodama, C., Seiki, T., Noda, A. T., Yamada, Y., Goto, D., Sawada, M., Miyoshi, T., Niwa, Y., Hara, M., Ohno, T., Iga, S., Arakawa, T., Inoue, T., and Kubokawa, H.: The Non-hydrostatic Icosahedral Atmospheric Model: description and development, Progress in Earth and Planetary Science, 1, 1–32, doi:10.1186/s40645-014-0018-1, 2014.

Sawa, Y., Machida, T., Matsueda, H., Niwa, Y., Tsuboi, K., Murayama, S., Morimoto, S., and Aoki, S.: Seasonal changes of CO_2, CH_4, N_2O, and SF_6 in the upper troposphere/lower stratosphere over the Eurasian continent observed by commercial airliner, Geophys. Res. Lett., 42, 2001–2008, doi:10.1002/2014GL062734, 2015.

Shanno, D. F. and Phua, K.-H.: Matrix conditioning and nonlinear optimization, Math. Program., 14, 149–160, doi:10.1007/BF01588962, 1978.

Takahashi, T., Sutherland, S. C., Wanninkhof, R., Sweeney, C., Feely, R. A., Chipman, D. W., Hales, B., Friederich, G., Chavez, F., Sabine, C., Watson, A., Bakker, D. C., Schuster, U., Metzl, N., Yoshikawa-Inoue, H., Ishii, M., Midorikawa, T., Nojiri, Y., Körtzinger, A., Steinhoff, T., Hoppema, M., Olafsson, J., Arnarson, T. S., Tilbrook, B., Johannessen, T., Olsen, A., Bellerby, R., Wong, C., Delille, B., Bates, N., and de Baar, H. J.: Climatological mean and decadal change in surface ocean pCO_2, and net sea-air CO_2 flux over the global oceans, Deep-Sea Research, Part II, 56, 554–577, 2009.

Thuburn, J.: Multidimensional Flux-Limited Advection Schemes, J. Comput. Phys., 123, 74–83, doi:10.1006/jcph.1996.0006, 1996.

Tomita, H. and Satoh, M.: A new dynamical framework of nonhydrostatic global model using the icosahedral grid, Fluid Dyn. Res., 34, 357–400, doi:10.1016/j.fluiddyn.2004.03.003, 2004.

Usui, N., Ishizaki, S., Fujii, Y., Tsujino, H., Yasuda, T., and Kamachi, M.: Meteorological Research Institute multivariate ocean variational estimation (MOVE) system: Some early results, Advances in Space Research, 37, 806–822, doi:10.1016/j.asr.2005.09.022, 2006.

Usui, N., Fujii, Y., Sakamoto, K., and Kamachi, M.: Development of a Four-Dimensional Variational Assimilation System for Coastal Data Assimilation around Japan, Mon. Wea. Rev., 143, 3874–3892, doi:10.1175/MWR-D-14-00326.1, 2015.

van der Werf, G. R., Randerson, J. T., Giglio, L., Collatz, G. J., Mu, M., Kasibhatla, P. S., Morton, D. C., DeFries, R. S., Jin, Y., and van Leeuwen, T. T.: Global fire emissions and the contribution of deforestation, savanna, forest, agricultural, and peat fires (1997–2009), Atoms. Chem. Phys., 10, 11707–11735, doi:10.5194/acp-10-11707-2010, 2010.

Yoshida, Y., Kikuchi, N., Morino, I., Uchino, O., Oshchepkov, S., Bril, A., Saeki, T., Schutgens, N., Toon, G. C., Wunch, D., Roehl, C. M., Wennberg, P. O., Griffith, D. W. T., Deutscher, N. M., Warneke, T., Notholt, J., Robinson, J., Sherlock, V., Connor, B., Rettinger, M., Sussmann, R., Ahonen, P., Heikkinen, P., Kyrö, E., Mendonca, J., Strong, K., Hase, F., Dohe, S., and Yokota, T.: Improvement of the retrieval algorithm for GOSAT SWIR XCO_2 and XCH_4 and their validation using TCCON data, Atoms. Meas. Tech., 6, 1533–1547, doi:10.5194/amt-6-1533-2013, 2013.

Yumimoto, K. and Takemura, T.: The SPRINTARS version 3.80/4D-Var data assimilation system: development and inversion experiments based on the observing system simulation experiment framework, Geosci. Model Dev., 6, 2005–2022, doi:10.5194/gmd-6-2005-2013, 2013.

Table 1. Prior and true flux datasets (other than the fossil fuel emission) used in the identical twin experiment

	Description	Reference
True	*Land:*	
	NEP fluxes from CASA modified by inversion	Randerson et al. (1997), Niwa et al. (2012)
	Biomass burning emissions from GFED v3.1	van der Werf et al. (2010)
	Ocean:	
	Climatological ΔpCO_2 measurement-based fluxes	Takahashi et al. (2009)
Priror	*Land:*	
	NBP fluxes from VISIT	Ito and Inatomi (2012)
	Ocean:	
	ΔpCO_2 measurement-based fluxes	Iida et al. (2015)

Table 2. List of the eight sensitivity tests and the global root mean square errors (GRMSE) of each posterior flux for the global land, the global ocean, and the global total. The numbers in parenthesis are those of the prior flux.

No.	Model	Optimization scheme	Prior error covariance	GRMSE [10^{-7} mol m^{-2} s^{-1}]		
				Land (5.58)	Ocean (0.24)	Global (5.59)
(1)	LINEAR	DR89	diag.	4.09	0.25	4.10
(2)	NON-LINEAR	DR89	diag.	6.69	0.36	6.70
(3)	LINEAR	POpULar	diag.	4.09	0.25	4.10
~~(4)~~	~~NON-LINEAR~~	~~POpULar~~	~~diag.~~	~~4.06~~	~~0.24~~	~~4.07~~
(5)	LINEAR	DR89	off-diag.	3.29	0.20	3.30
(6)	NON-LINEAR	DR89	off-diag.	3.37	0.20	3.37
(7)	LINEAR	POpULar	off-diag.	3.29	0.20	3.30
(8)	NON-LINEAR	POpULar	off-diag.	3.20	0.20	3.21
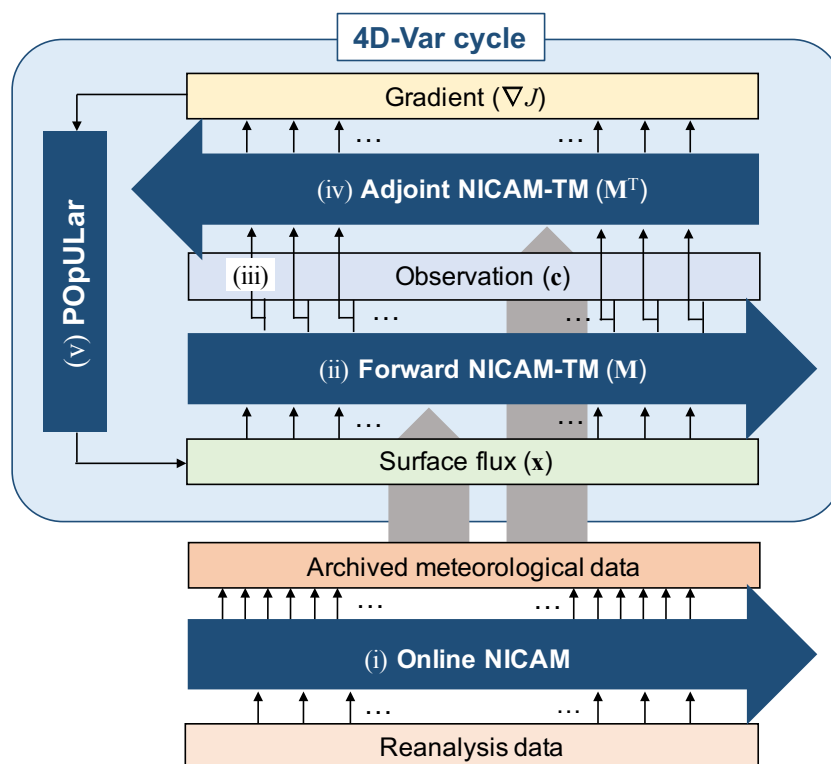
Figure 1. A schematic figure of NICAM-TM 4D-Var. A roman numeral indicates each calculation described in the text.
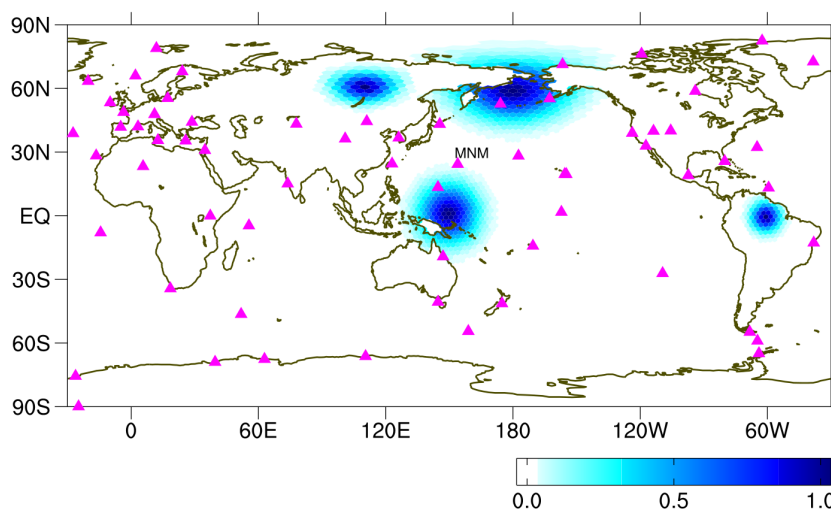
Figure 2. Locations of surface flask observation site (magenta triangle) and four distributions of error correlation introduced in the off-diagonal elements of **B**, which are centered at two land grids (60°N, 110°E and 60°N, 180°), and two ocean grids (0°, 150°E and 0°, 60°W), selected for example.
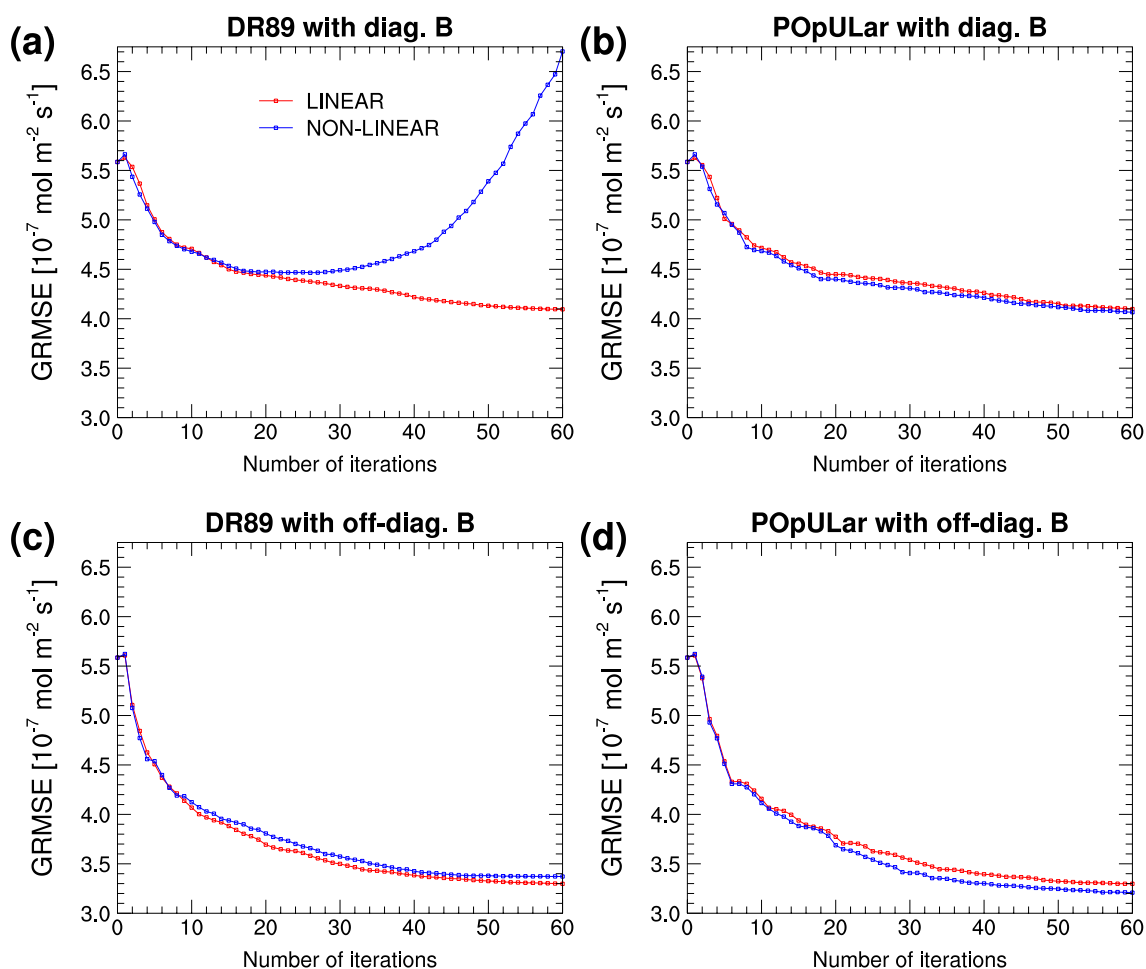
Figure 3. Global root-mean-square error (GRMSE) changes with iterations for the linear (red) and non-linear (blue) models. Sensitivities to the optimization schemes (DR89: left, POpULar: right) and to the prior error covariance matrixes (diagonal: upper, off-diagonal: bottom) are shown.
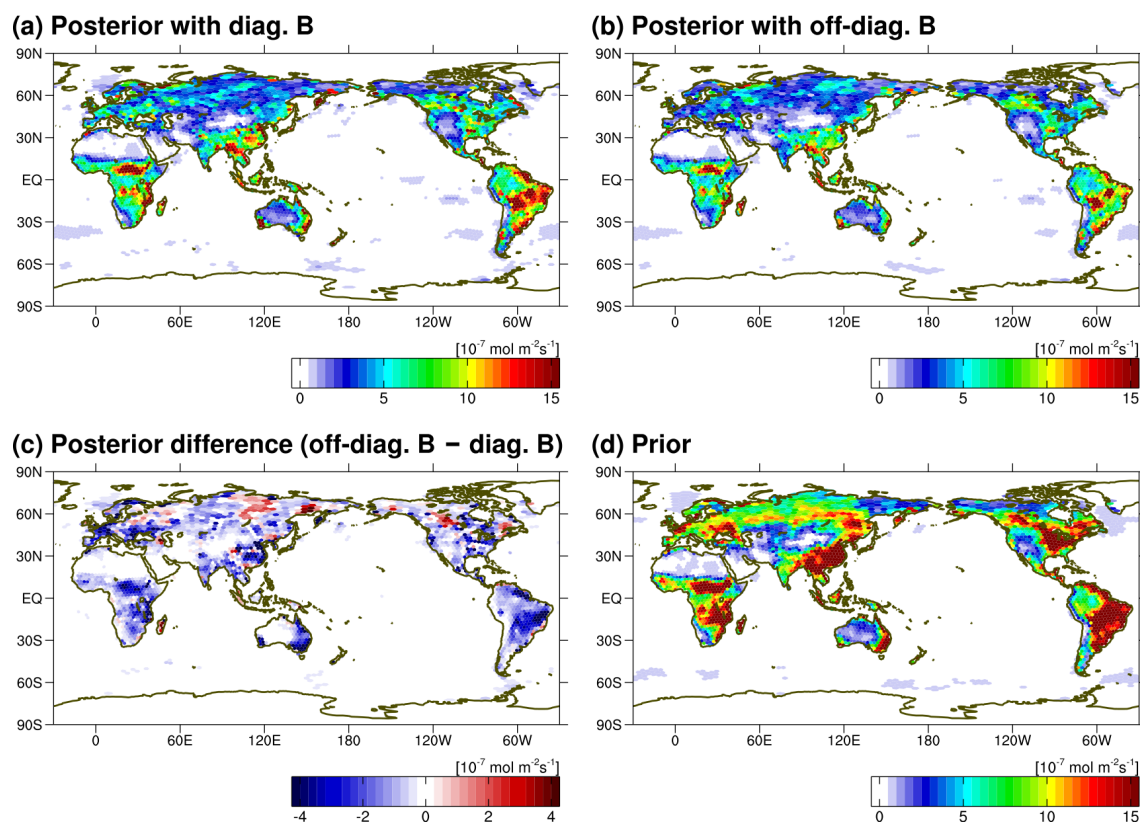
Figure 4. Root-mean-square error (RMSE) distributions of the posterior fluxes derived by POpULar+NON-LINEAR with the diagonal **B** (a) and the off-diagonal **B** (b). The difference between (b) and (a) is shown in (c) as well as the RMSE distribution of the prior flux (d).
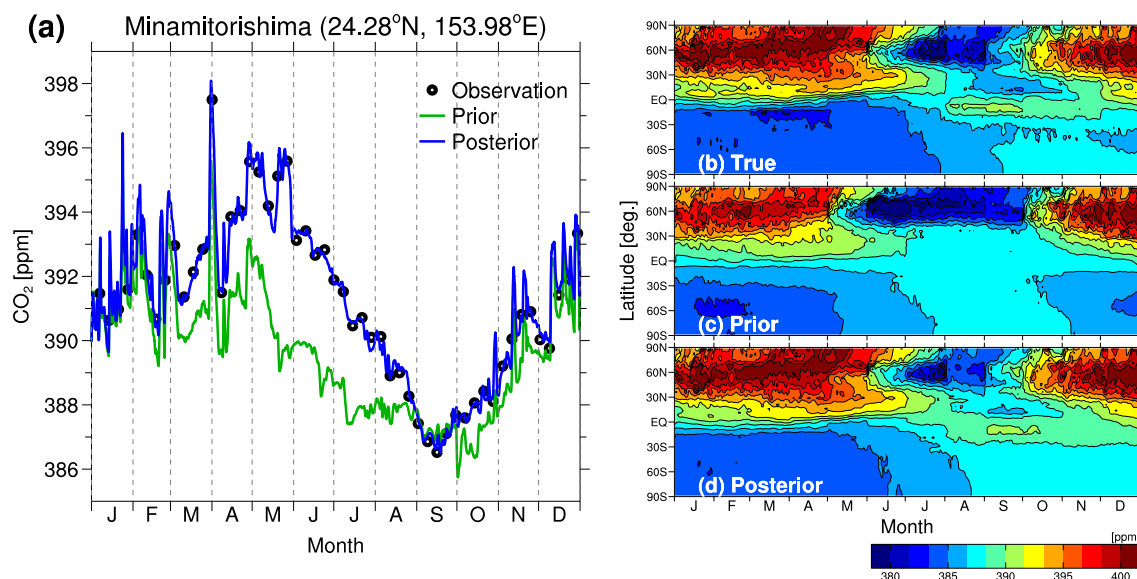
Figure 5. Atmospheric CO_2 concentrations simulated by the forward NICAM-TM driven by the true, prior and posterior fluxes. The left panel shows the time series of concentrations at one observation site (Minamitorishima), located in the western North Pacific. Black open circles denote observations that are assimilated in the experiment, and green and blue lines represent CO_2 concentrations calculated from the prior and posterior fluxes, respectively. The right panel shows latitude-time cross sections of surface zonal averages calculated from the true (b), prior (c), and posterior fluxes (d).
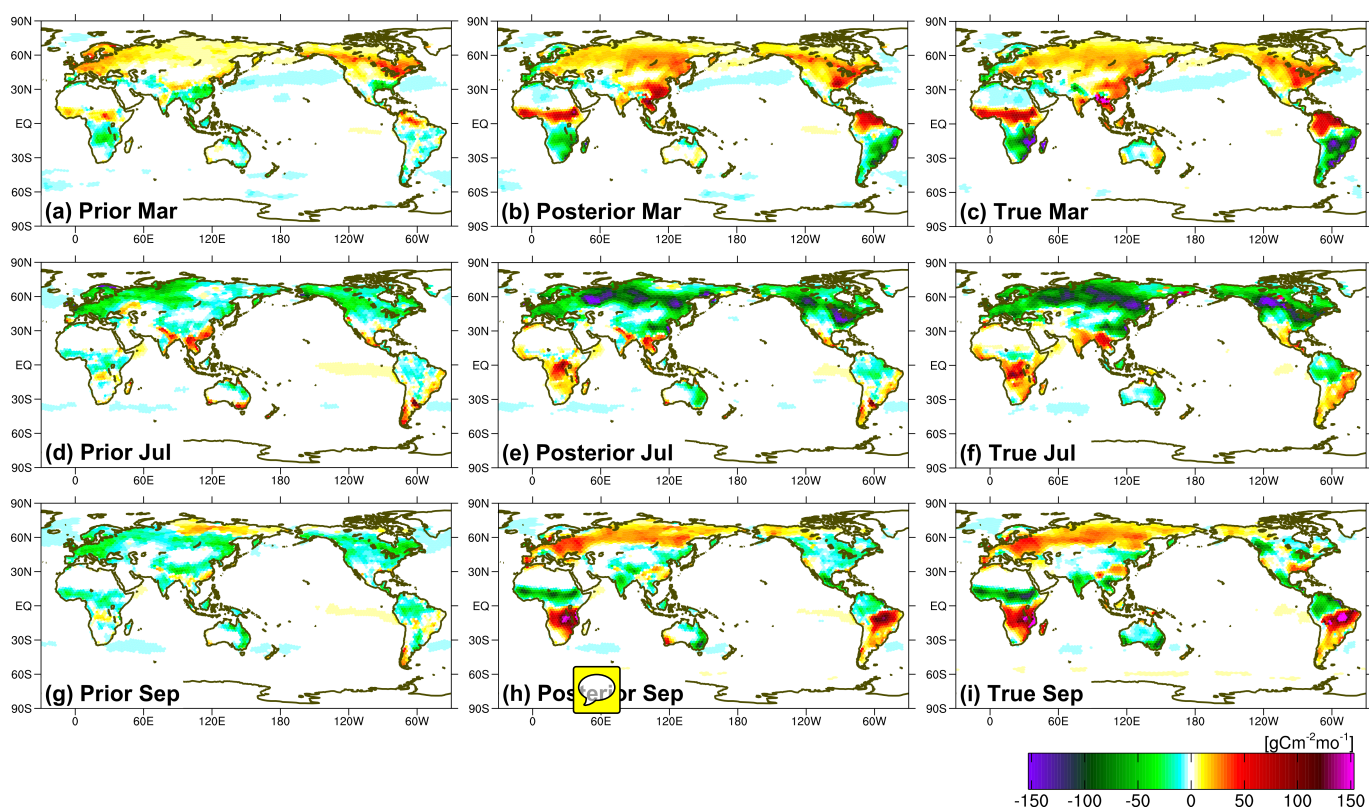
Figure 6. Monthly mean distributions of the prior (left), posterior (middle) and true (right) CO_2 fluxes. Fluxes are shown for March (a-c), July (d-f) and September (g-i) of 2010. Note that the fluxes do not include fossil fuel emissions, which are not optimized in the inversion.
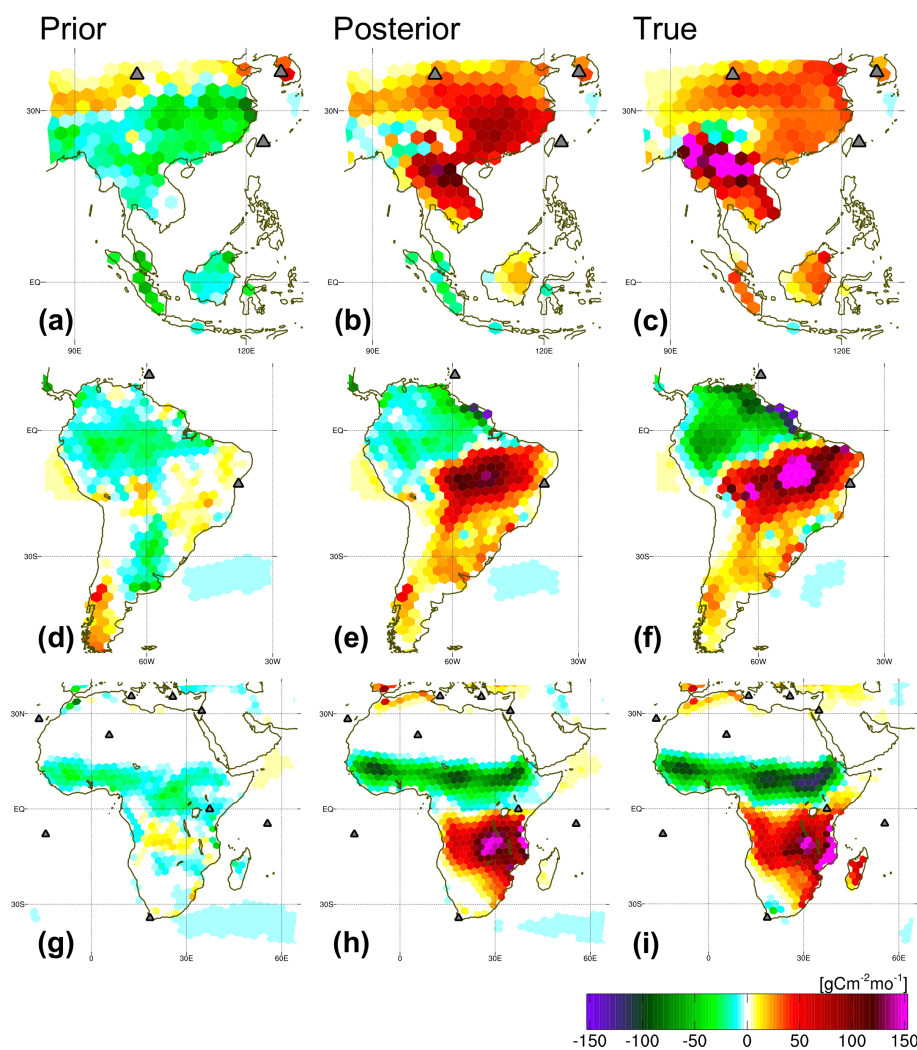
Figure 7. Same as Fig. 6, but focused on regional flux anomalies due to biomass burnings for Southeast Asia in March (a-c), South America in September (d-f), and Africa in September (g-i). Gray triangles denote locations of the observational sites.
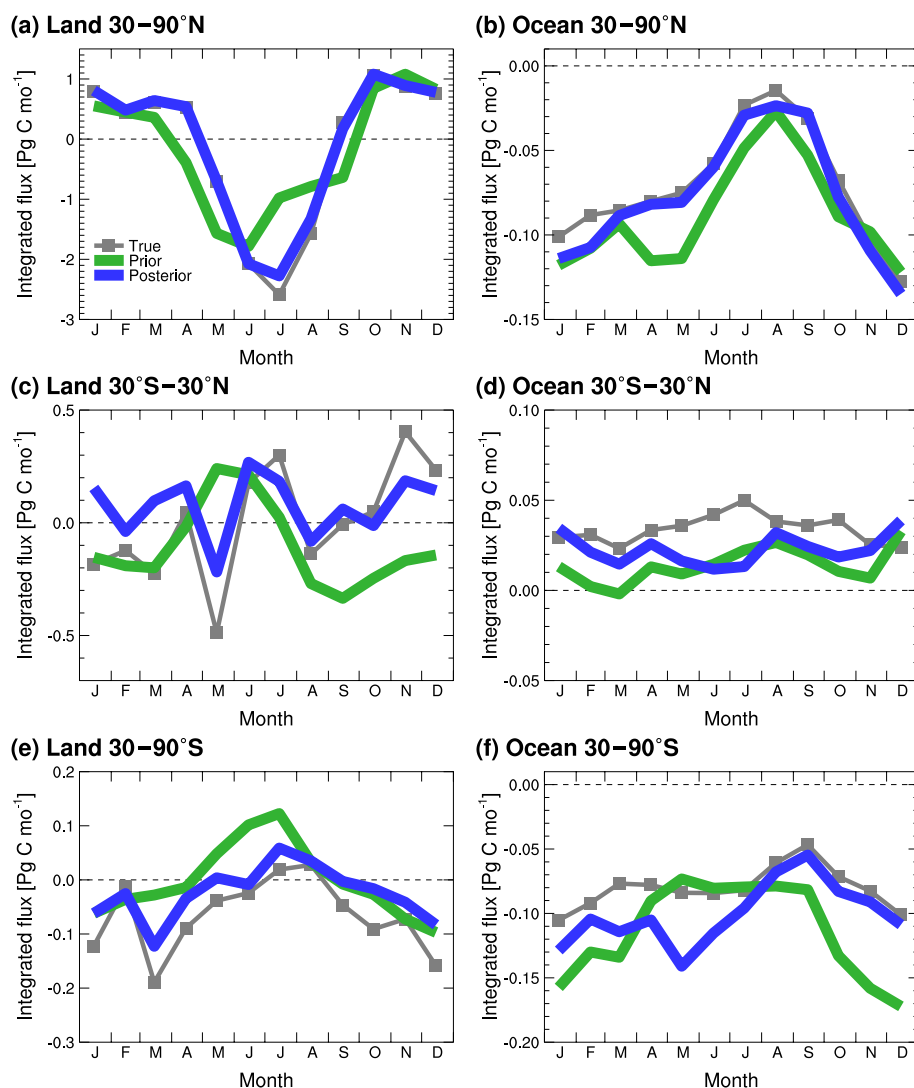
Figure 8. Monthly variations of the true (gray), prior (green) and posterior (blue) CO_2 fluxes integrated for latitude bands of 30–90°N (a,b), 30°S–30°N (c,d) and 30-90°S (e,f). Terrestrial (non-fossil fuel flux) (right) and ocean (left) fluxes are separately shown.
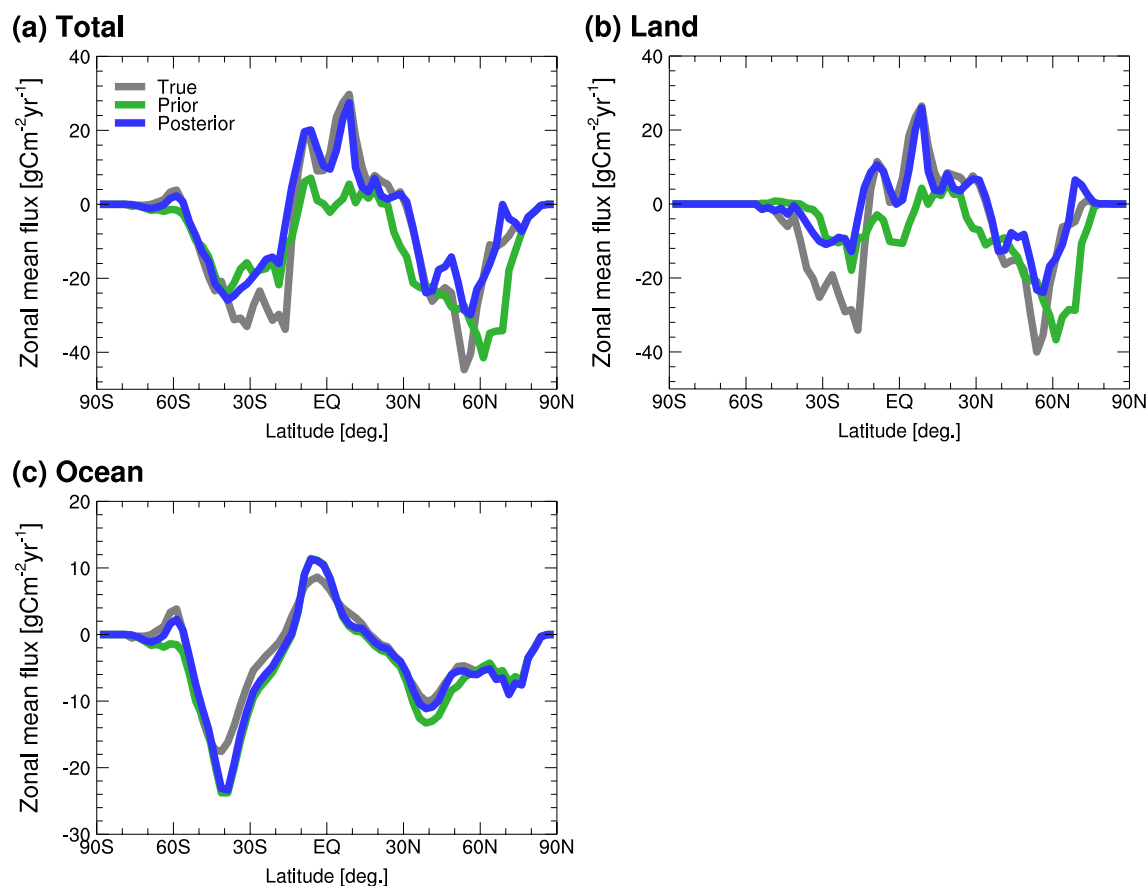
Figure 9. Latitudinal profiles of annual zonal mean CO_2 fluxes (gray: true, green: prior, blue: posterior), for the total (a), terrestrial (b) and ocean (c) areas. Note that fossil fuel emission is not included.